EXPERIMENTAL AND NUMERICAL PROGRESSIVE FAILURE ANALYSIS OF CORRUGATED CORE TYPE COMPOSITE SANDWICH STRUCTURE

by

Emre Çalık

B.S., Mechanical Engineering, Boğaziçi University, 2014

Submitted to the Institute for Graduate Studies in
Science and Engineering in partial fulfillment of
the requirements for the degree of
Master of Science

Graduate Program in Mechanical Engineering
Boğaziçi University

2018

EXPERIMENTAL AND NUMERICAL PROGRESSIVE FAILURE ANALYSIS OF CORRUGATED CORE TYPE COMPOSITE SANDWICH STRUCTURE

APPROVED BY:

Prof. Nuri Ersoy (Thesis Supervisor)	.....
Prof. Fazıl Önder Sönmez	.....
Assist. Prof. Alpay Oral	.....

DATE OF APPROVAL: 17.09.2018

ACKNOWLEDGEMENTS

First of all, I would like to express my appreciation to my thesis supervisor Prof. Nuri Ersoy for his support, guidance and patience during my master thesis.

I am also thankful to my committee members, Prof. Fazıl Önder Sönmez and Assist. Prof. Alpay Oral for their comments and constructive critics.

I also thank my friends and colleagues Sina Ahmadvashaghbash and Fatih Öz for their assistance throughout my study.

Special thanks to Hüseyin Demircioğlu for his great support and motivation. He was always there to help me no matter what the problem was and what I had been going through.

Last but definitely not the least, I am grateful to my parents, Fatma-Hasan Çalık and my sister Beyza Çalık for their trust, support and understanding.

ABSTRACT

EXPERIMENTAL AND NUMERICAL PROGRESSIVE FAILURE ANALYSIS OF CORRUGATED CORE TYPE COMPOSITE SANDWICH STRUCTURE

The demand in industry for composite sandwich structures has been rising thanks to their superior material properties and design flexibility. It is possible to design a composite sandwich structure special to any operating condition by changing its geometry, stacking sequence, fibre direction, material, etc. Therefore, there are limitless options to design the most functional composite structure by meeting operational requirements. The impact of each design parameter must be investigated during development studies. Conducting experiments is a reliable way of doing this but it is also very costly and time consuming. By using Finite Elements Methods, behaviour of the composite structure can be predicted without carrying out experiments. In this way, development cost and time can be dramatically reduced.

The aim of this study is to investigate the failure mechanisms of a corrugated core type composite sandwich structure under quasi-static loading condition. Chosen corrugated core type structure has a novel geometry and ply sequence. In this design, AS4/8552 prepreg material is used for both of core and facesheets in a single process to eliminate the need for secondary bonding operations. Finite Element Analysis (FEA) is performed by using ABAQUS software to predict failure responses of the structure. Hashin Failure Criterion is used to predict intralaminar damage modes and Cohesive Zone Model is utilized to simulate the interlaminar damage. Four-point bending and compression tests are also carried out to investigate the post-failure behaviour of the structure and to check the correlation between simulation and experiment.

ÖZET

KORÜGE TİPİ KOMPOZİT SANDVİÇ YAPININ DENEYSEL VE NUMERİK İLERLEMELİ HASAR ANALİZİ

Kompozit sandviç yapılar üstün özellikleri sayesinde endüstride giderek daha çok tercih edilmektedir. Geometri, malzeme, tabaka dizilimi ve fiber açısı değiştirilerek özgün sandviç yapılar tasarlamak mümkündür. Dolayısıyla, belirli bir kullanım alanına yönelik sandviç yapı tasarlamanın sayısız yolu vardır. Geliştirme çalışmaları sırasında, bu tasarım parametrelerinin nihai yapı üzerindeki etkisi incelenmeli ve yapının hasar mekanizmaları belirlenmelidir. Bunun en geçerli yolu nihai yapıyı üretip test yapmaktır. Fakat, test çalışmaları yüksek maliyetli ve zaman alıcı süreçlerdir. Sonlu Elemanlar Yöntemi kullanılarak da sandviç yapının çalışma koşullarındaki davranışı incelenebilir ve geliştirilmesi gereken parametreler belirlenebilir. Bu yöntem teste göre hem daha az maliyetlidir hem de daha az vakit alır.

Bu çalışmanın amacı, korüge tipi kompozit sandviç yapıların yarı statik yük altındaki ilerlemeli hasar analizini yapmaktır. Çalışma kapsamında seçilen korüge tipi sandviç yapısı özgün bir geometriye ve tabaka dizilimine sahiptir. Yapı, AS4/8552 prepreg malzemesinden tek bir proses ile üretilmiş, böylece ikincil yapıştırma işlemi elimine edilmiştir. Yapının hasar davranışı Sonlu Elemanlar Yöntemi kullanılarak ABAQUS programında incelenmiştir. Tabaka içi hasarlar için Hashin kriteri kullanılmış olup tabakalar arası delaminasyonu içeren hasar mekanizması için Kohesiv Alan Modeli tanımlanmıştır. Sonlu Elemanlar Analizi sonuçlarını doğrulamak ve sandviç yapının hasar mekanizmalarını incelemek için basma ve dört noktalı bükme testleri gerçekleştirilmiştir.

TABLE OF CONTENTS

ACKNOWLEDGEMENTS . . . iii
ABSTRACT . . . iv
ÖZET . . . v
LIST OF FIGURES . . . vii
LIST OF TABLES . . . xii
LIST OF SYMBOLS . . . xiii
LIST OF ACRONYMS/ABBREVIATIONS . . . xvi
1. INTRODUCTION . . . 1
2. THEORY . . . 4
2.1. Composite Sandwich Structure . . . 4
2.2. Failure Modes . . . 14
2.2.1. Failure Modes of Composite Materials . . . 14
2.2.2. Failure Modes of Sandwich Structures . . . 16
2.3. Progressive Failure Analysis . . . 17
2.3.1. Intralaminar Failure Analysis . . . 18
2.3.1.1. Damage Initiation . . . 19
2.3.1.2. Damage Evolution . . . 25
2.3.2. Interlaminar Failure Analysis . . . 29
2.3.3. Modelling Progressive Failure Analysis in ABAQUS . . . 35
2.4. Objectives . . . 41
3. NUMERICAL ANALYSIS . . . 42
4. EXPERIMENTAL STUDY . . . 48
4.1. Specimen Preparation . . . 48
4.2. Test Procedure . . . 50
5. RESULTS AND DISCUSSION . . . 52
5.1. Compression Test and FEA . . . 52
5.2. Four-Point Bending Test and FEA . . . 57
6. CONCLUSIONS AND FUTURE WORK . . . 71
REFERENCES . . . 72

LIST OF FIGURES

Figure 1.1. Emission reduction targets in the global automotive industry [2] . 1

Figure 1.2. Materials used in Boeing-787 Dreamliner [4] 2

Figure 2.1. Sandwich structure and I-beam geometry [8] 4

Figure 2.2. Composite sandwich structure core types [9] 5

Figure 2.3. 2-D truss core type, shear test failure modes [10] 6

Figure 2.4. Graded lattice core buckling failure [11] 6

Figure 2.5. (a) Aluminum corrugation (b) GFRP corrugation (c) CFRP corrugation [12] 7

Figure 2.6. (a) Progressive failure development of CFRP corrugation (b) Damage modes of CFRP corrugation [12] 7

Figure 2.7. Configuration of a novel 3D corrugated core composite sandwich structure [13] 8

Figure 2.8. Failure mode of 3D corrugated core composite sandwich structure with (a) small graded parameters (b) large graded parameters [13] 8

Figure 2.9. Progressive failure behaviour of (a) hybrid composite structure (b) carbon fiber composite structure [14] 9

Figure 2.10. Foam filled composite sandwich structure [15] 10

Figure 2.11. Compressive behaviour of foam filled structure with lattice web [15] 10

Figure 2.12. Sandwich panel with kagome lattice core [16] 11

Figure 2.13. Buckling failure in woven core [17] 12

Figure 2.14. Pyramidal lattice truss panel [18] 12

Figure 2.15. a) Schematic representation of the first lay-up method, b) Schematic representation of the second lay-up method [19] 13

Figure 2.16. Fibre failure modes: (a) Shear fibre failure under compression load in fibre direction (b) Tensile fibre failure under tensile load in fibre direction [20] 14

Figure 2.17. Matrix failure modes: (a) Shear matrix failure under compression load in transverse direction (b) Tensile matrix failure under tensile load in transverse direction [20] 14

Figure 2.18. Shear failure in the 2-3 plane [20] 15

Figure 2.19. Failure in shear in the 1-2 plane [20] 15

Figure 2.20. Delamination failure [21] 16

Figure 2.21. Sandwich structure failure modes [24] 17

Figure 2.22. Typical stress-strain curve of a metal specimen [26] 19

Figure 2.23. Material principal coordinate system 19

Figure 2.24. Typical material response showing progressive damage [26] 26

Figure 2.25. Equivalent stress-displacement curve [30] 27

Figure 2.26. Damage variable as a function of equivalent displacement [30] . . . 29

Figure 2.27. Bilinear form of traction-separation law [31] 31

Figure 2.28. Failure modes [31] 31

Figure 2.29. Mixed-mode response in cohesive interactions [32] 33

Figure 2.30. Sokolinsky corrugated composite model top view [35] 36

Figure 2.31. Cohesive zone elements and delamination in DCB [39] 37

Figure 2.32. The effect of different element lengths on damage simulation [40] . 38

Figure 2.33. The effect of artificial interfacial fracture strength [36] 39

Figure 2.34. The effect of penalty stiffness on simulation accuracy and number of iterations [43] 40

Figure 2.35. Comparison between prediction and test results [44] 41

Figure 3.1. Cross section of four-point bending test model 42

Figure 3.2. Cross section of compression test model 43

Figure 3.3. Boundary conditions of four-point bending test model 46

Figure 3.4. Boundary conditions of compression test model 46

Figure 3.5. Deltoid section 47

Figure 4.1. Schematic representation of lay-up 49

Figure 4.2. Curing cycle for AS4/8552 49

Figure 4.3. Compression test sample (dimensions in mm) 50

Figure 4.4. Four-point bending test sample (dimensions in mm) 50

Figure 4.5. Compression test setup 51

Figure 4.6. Four-point bending test setup 51

Figure 5.1. Failures in 1st compression test 52

Figure 5.2. Failures in 2nd compression test 53

Figure 5.3. Delamination and Hashin's fibre compressive damage 54

Figure 5.4. Delamination and Hashin's matrix compressive damage 55

Figure 5.5. Load-displacement curves obtained in compression tests and FEA simulation 56

Figure 5.6. Failures in 1st four-point bending test 59

Figure 5.7. Failures in 2nd four-point bending test 61

Figure 5.8. Delamination and matrix tensile damages in 4-point bending test simulation 65

Figure 5.9. Delamination and fibre tensile damages in 4-point bending test simulation 68

Figure 5.10. Load-displacement curves obtained in 4-point bending tests and FEA simulation 69

LIST OF TABLES

Table 3.1. Material properties of AS4/8552 [46] 44

Table 3.2. Interlaminar properties of AS4/8552 45

LIST OF SYMBOLS

C_d	Damaged elasticity matrix
D	Damage parameter
d_f	Current state of fibre damage
d_m	Current state of matrix damage
d_s	Current state of shear damage
d_f^T	Tensile fibre damage variable
d_f^C	Compressive fibre damage variable
d_m^T	Tensile matrix damage variable
d_m^C	Compressive matrix damage variable
E_{11}	Elastic modulus in fibre direction
E_{22}	Elastic modulus in transverse direction
E_{33}	Elastic modulus through-the-thickness direction
G_1	Strain energy release rate in mode–I
G_2	Strain energy release rate in mode–II
G_3	Strain energy release rate in mode–III
G_C	Mixed Mode Critical Fracture Energy
G_n	Fracture energy in mode–I
G_s	Fracture energy in mode–II
G_t	Fracture energy in mode–III
G_n^C	Critical fracture energy in mode–I
G_s^C	Critical fracture energy in mode–II
G_t^C	Critical fracture energy in mode–III
K_n	Penalty stiffness in mode–I
K_s	Penalty stiffness in mode–II
K_t	Penalty stiffness in mode–III
M	Damage operator
N_e	Number of elements in cohesive zone
t	Lamina thickness

α	Energy law parameter
β	Penalty stiffness parameter
δ_n	Critical separation distance in mode–I
δ_s	Critical separation distance in mode–II
δ_t	Critical separation distance in mode–III
ϵ	Strain tensor
ι_e	Mesh size
ι_{cz}	Cohesive zone length
ν	Poisson's ratio
σ_1^C	Compressive strength in fibre direction
σ_1^T	Tensile strength in fibre direction
σ_2^C	Compressive strength in transverse direction
σ_2^T	Tensile strength in transverse direction
σ_1	Normal stress in fibre direction
σ_2	Normal stress in transverse direction
σ_3	Normal stress in through-the-thickness direction
σ_{1U}	Tensile or compressive strength in fibre direction
σ_{2U}	Tensile or compressive strength in transverse direction
σ_{true}	True stress
σ^Y	Yield strength
τ_{12}	Shear stress in plane–12
τ_{13}	Shear stress in plane–13
τ_{23}	Shear stress in plane–23
τ_{12}^L	Longitudinal shear strength in plane–12
τ_{12}^T	Transverse shear strength in plane–12
τ_{12}^F	Longitudinal or transverse shear strength in plane–12
τ_n^0	Interfacial fracture strength in mode–I
τ_s^0	Interfacial fracture strength in mode–II
τ_t^0	Interfacial fracture strength in mode–III
$\overline{\tau}^n$	Undamaged stress at contact point in mode–I
$\overline{\tau}^s$	Undamaged stress at contact point in mode–II

$\overline{\tau}^t$	Undamaged stress at contact point in mode–III
$\overline{\tau}^o$	Artificial interfacial fracture strength

LIST OF ACRONYMS/ABBREVIATIONS

2D	Two dimensional
3D	Three dimensional
BK	Benzeggagh-Kenane
C3D8R	Solid element
CAGR	Compound annual growth rate
CFRP	Carbon fibre reinforced polymer
CZM	Cohesive zone model
DCB	Double cantilever beam
ENF	End-notch flexure
FE	Finite element
FEA	Finite element analysis
FEM	Finite element method
GFRP	Glass fibre reinforced polymer
IWLSC	Integrated woven lattice sandwich composite
LEFM	Linear elastic fracture mechanism
SC8R	Continuum shell element
VARTM	Vacuum assisted resin transfer molding

1. INTRODUCTION

Composite sandwich structures have been more desirable and their applications have been dramatically increasing in a wide range of industries such as aerospace, aviation, automotive, marine, power systems, etc. Their superior material properties such as high stiffness/strength to weight ratio and high corrosion resistance stand out as the key drivers behind this trend. Especially aerospace and automotive industries are continuously in search of using lighter materials to increase fuel efficiency, reduce weight and achieve carbon emission targets.

In automotive industry, as it is illustrated in Figure 1.1, countries set targets for automotive companies to reduce carbon emission. For example, while the average emission level of a new car sold in 2016 was 120 g/km, EU sets new target to reduce carbon emission for a new car to the level of 95 g/km by 2021 [1]. This refers to the reduction of 40% compared to the fleet average carbon emission level of 160 g/km in 2007 [2]. The easiest way of achieving this target is to reduce fleet weight, so the demand for lightweight materials in the global automotive industry is increasing. It is expected that the lightweight materials market in automotive industry will reach 335 billion dollars in 2025 by growing at a compound annual growth rate (CAGR) of 7% [2].

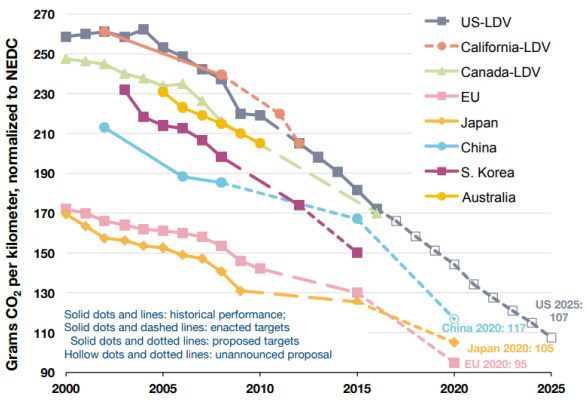


Figure 1.1: Emission reduction targets in the global automotive industry [2]

The demand in aerospace industry for advanced composite materials is also rising. For example, the composite content in commercial aircrafts such as Boeing-787 Dreamliner and Airbus A-350 has now increased to 50% by weight while it was only 5% in 1990s [3]. Figure 1.2 shows materials used in Boeing-787 Dreamliner aircraft [4]. In this industry, reduced weight is not the only driver behind this trend. Assembly simplification and high corrosion resistance are also very crucial benefits of composite structures. It is expected that the demand for composite materials will continue increasing in construction and wind energy industries as well. As a matter of fact, the forecasted CAGR of composite market is 8,3% until 2021 [5].

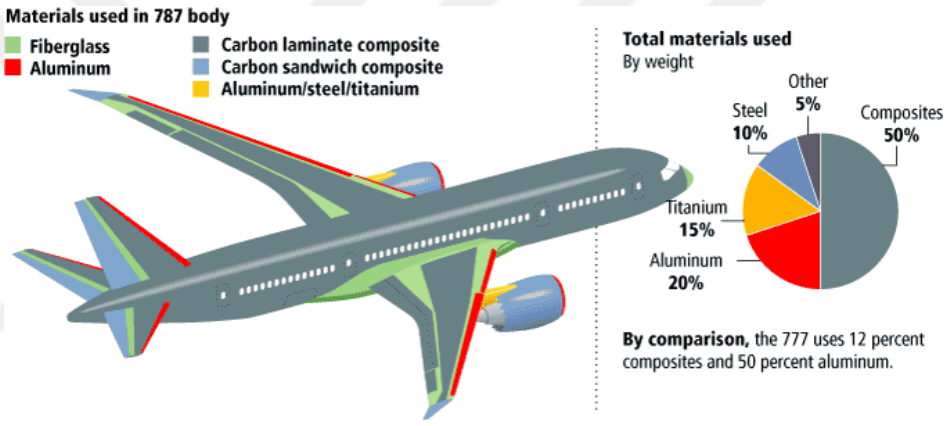


Figure 1.2: Materials used in Boeing-787 Dreamliner [4]

Considering that composite sandwich structures are made up of a combination of different laminates and each laminate can have different lay-up sequences, there are limitless options to design a special sandwich structure. Any variation in lay-up sequence, laminate combination and structure geometry has huge impact on overall material properties. Therefore, there are numerous ongoing research and development efforts on this topic to obtain even more superior material properties depending on application of the related structure and to make the design more reliable by predicting its response under different loading conditions.

A typical composite sandwich structure is comprised of two layers and a core inserted in between these layers. These structures can be classified according to their core types [6]: Foam cores, textile cores, corrugated cores, honeycomb cores, etc. Core type and the way it supports facesheets are the main parameters which determine capability of sandwich structure.

All development studies in mechanical design require validation before introducing the new concept to industrial applications. The traditional way of validation is to conduct tests and optimize the design parameters depending on test results. This iteration process is highly costly and time consuming so that new design benefits might not even cover development cost. One alternative way of validation is to conduct Finite Element Analysis (FEA). FEA tools help to simulate the effects of loads, vibration, heat and fluids on the structure. By using Finite Element Methods, experiments are not needed in every sub-steps of development studies. This would decrease cost and time.

The purpose of this study is to investigate failure behaviour of a corrugated core type composite sandwich structure. First of all, failure of a structure refers to its inability to carry load. Although a structure is exposed to excessive deformation, it might still carry load and be functional. Therefore, it is quite crucial to understand and predict response of a structural component before the failure reaches to a catastrophic level. There are some theories developed to explain and understand failure process of composite structures. In this way, it is possible to predict whether structure is safe from catastrophic failure or not. In this study, Hashin Failure Criterion is used to simulate intralaminar damages. Furthermore, Cohesive Zone Model is defined to simulate interlaminar failures in the structure.

2. THEORY

2.1. Composite Sandwich Structure

Composite materials are consisted of two or more materials combined on a macro scale so that the resulting material has better capabilities than the constituent materials alone. They offer many improved properties such as high stiffness, high strength, high corrosion resistance, low weight, high fatigue life, etc. There are three main composite types: fibrous composites that consist of fibres in a matrix, particulate composites that consist of one material in matrix of another and laminated composites that consist of layers of different materials [7].

Composite sandwich structure is a laminated type composite and its geometry resembles to an I-beam (see Figure 2.1). It is typically composed of two thin and stiff facesheets bonded to a relatively thick and light core. This type of structure has high stiffness to weight ratio compared to monocoque structures. Bending loads are carried by facesheets whereas core section supports shear forces.

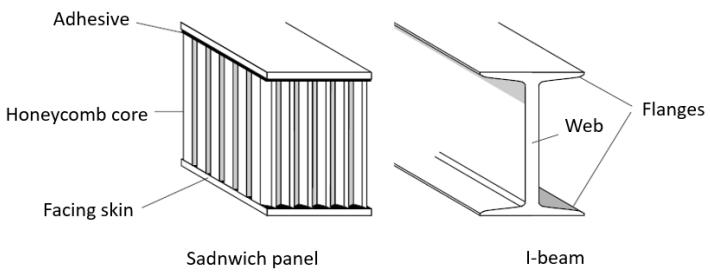


Figure 2.1: Sandwich structure and I-beam geometry [8]

Sandwich structures are classified according to their core types. Figure 2.2 shows the most common composite sandwich cores [9]. In this study, only corrugated core type sandwich structure is investigated. In this type, core laminates elongate along the longitudinal or transverse direction.

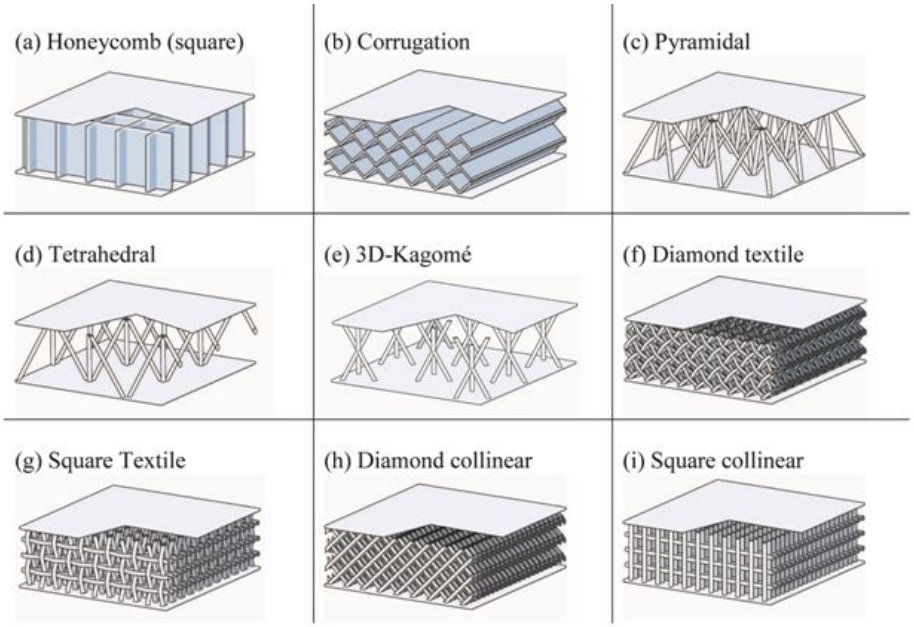


Figure 2.2: Composite sandwich structure core types [9]

There are several studies on functional novel cores in composite sandwich structures that has advantages as compared to conventional honeycomb or foam core. Hollow functional cores are preferred since they allow an empty space between facesheets and it can be utilized for other purposes such as cabling, thermal managements, etc.

Wang et al. [10] developed a 2-D truss core design manufactured based on hot-pressing method. Both ends of 2-D truss core were inserted into the facesheets during prepreg laying process. The structure was investigated under out-of-plane compression, shear and three-point bending tests. Wang concluded that the shear strength of the core was higher than the interface strength of facesheets but the delamination occured on the area where truss core and facesheets are embedded to each other (see Figure 2.3).

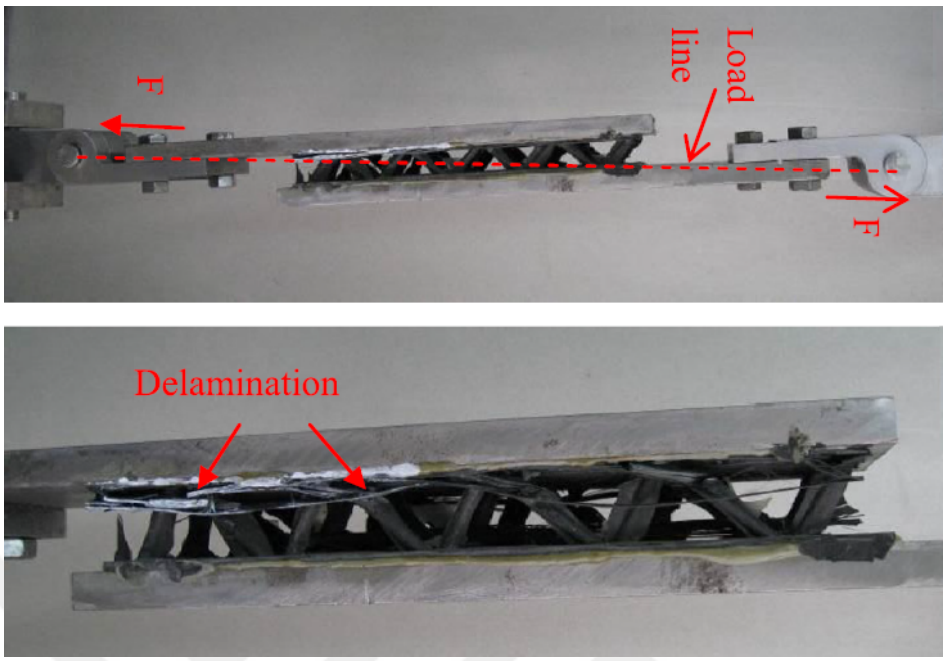


Figure 2.3: 2-D truss core type, shear test failure modes [10]

In another study, Xu et al. [11] suggested to use a graded form of the lattice cores, which means that the core geometry change along the longitudinal direction. The structure was optimized so that core ribs are more dense around the areas which are supposed to carry more load. The structural performance of this design was investigated under three-point bending test. As shown in Figure 2.4, core buckling was the main failure mechanism of this design under three-point bending loads.

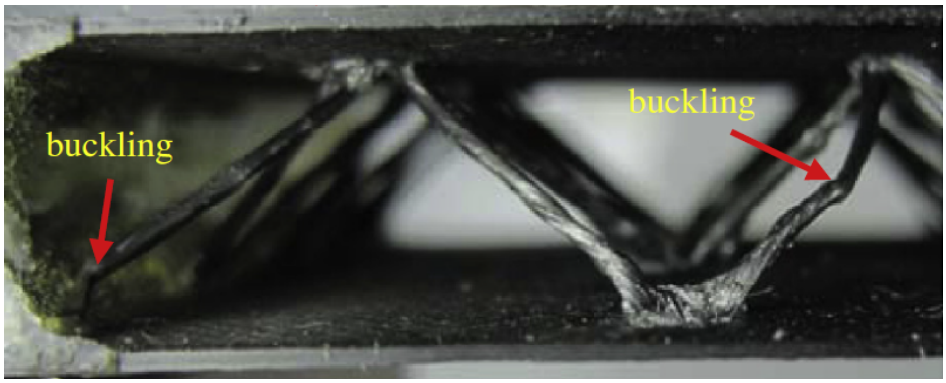


Figure 2.4: Graded lattice core buckling failure [11]

Rejab et al. [12] developed a triangular corrugated core using 45° profiled mould design. Cores were fabricated by hot-pressing method and then bonded to facesheets. As it is illustrated in Figure 2.5, three different structures were manufactured depending on materials: Aluminum alloy, glass fibre reinforced plastic (GFRP) and carbon fibre reinforced plastic (CFRP). Their failure behaviours were investigated under compression loads both experimentally and numerically. It was observed that initial failure was dominated by rib buckling for all three structures. Beyond that, plastic deformation occured in core section of aluminum structure whereas fibre fracture, delamination and debonding failures took place in core section of GFRP and CFRP structures (see Figure 2.6).

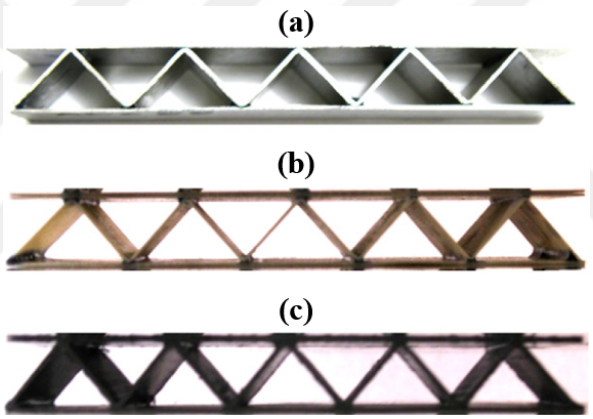


Figure 2.5: (a) Aluminum corrugation (b) GFRP corrugation (c) CFRP corrugation [12]

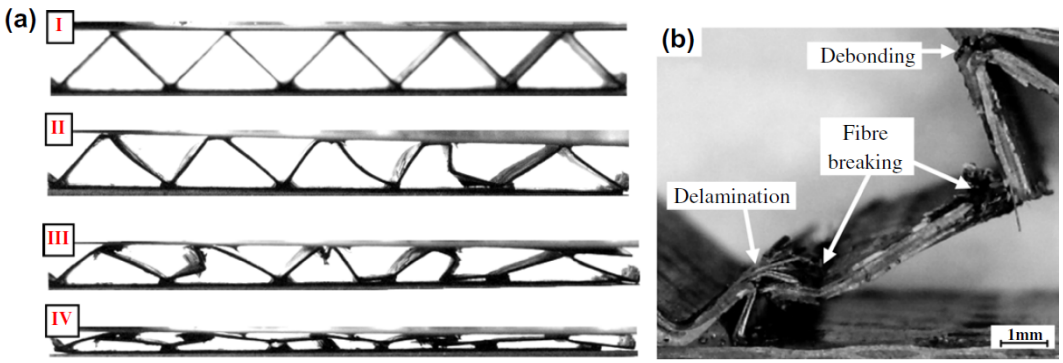


Figure 2.6: (a) Progressive failure development of CFRP corrugation (b) Damage modes of CFRP corrugation [12]

In another study, Xu et al. [13] developed and fabricated a novel 3D corrugated core sandwich structure (see Figure 2.7). The effects of facesheet thickness and graded web parameters such as trapezoid web upper thickness (b_u) and trapezoid web bottom thickness (b_d) were investigated in terms of failure behaviour under compression and bending loads. Under compression, it was observed that fracture of the core was the main failure mode of the structure with small graded parameters while core buckling was the main failure mode of the structure with large graded parameters (see Figure 2.8). Furthermore, it was concluded that graded web parameters had negligible impact on the bending strength of the structure with thin facesheet whereas they had significant effect on the structure with thick facesheet.

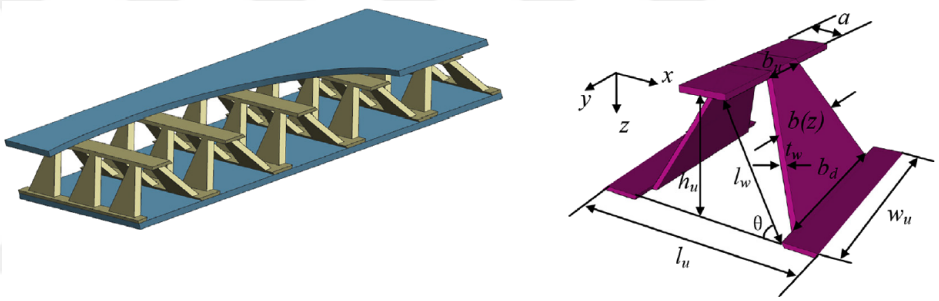


Figure 2.7: Configuration of a novel 3D corrugated core composite sandwich structure [13]

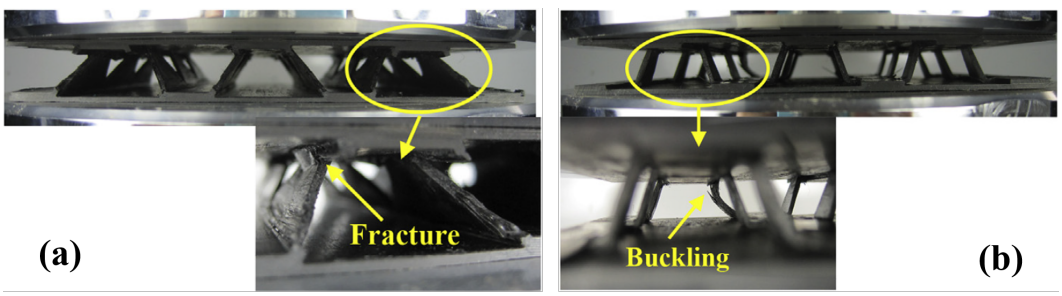


Figure 2.8: Failure mode of 3D corrugated core composite sandwich structure with (a) small graded parameters (b) large graded parameters [13]

Jin et al. [14] investigated the impact of design parameters such as corrugation angle, core thickness and fibre type on energy absorption capacity of corrugated core composite sandwich structure.

After conducting compression and three-point bending tests, it was observed that hybridization of glass and carbon fibres (50:50) in facesheets resulted in similar energy absorption capacity as the facesheets fabricated from entirely carbon fibre. Progressive failure behaviour of these structures under compression loads is illustrated in Figure 2.9. It was also concluded that increasing corrugation angle and core thickness improved bending strength of the structure.

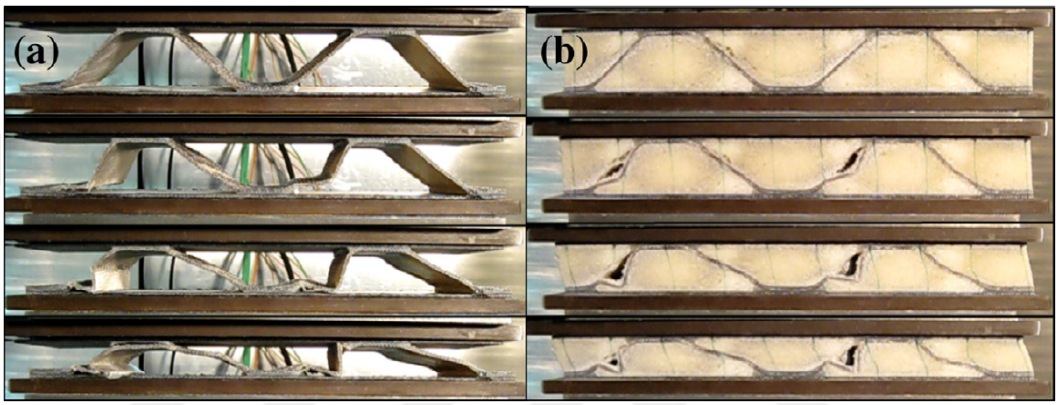


Figure 2.9: Progressive failure behaviour of (a) hybrid composite structure (b) carbon fiber composite structure [14]

In another study, Wu et al. [15] proposed a novel foam filled composite structure (see Figure 2.10) to improve energy absorption capacity and peak strength. In this design, lattice webs were used between foam-filled core sections. The effects of foam density, lattice web spacing and lattice web thickness were investigated by conducting compression tests. As it is illustrated in Figure 2.11, web buckling was the main failure mode under compression loads. Results also showed that using lattice webs between foam cores increased peak strength of the structure 1600% compared to conventional foam filled only composite structures. Furthermore, thicker lattice web thickness with small lattice web spacing increased energy absorption capacity of the structure. It was also concluded increasing foam density had small impact on peak strength.

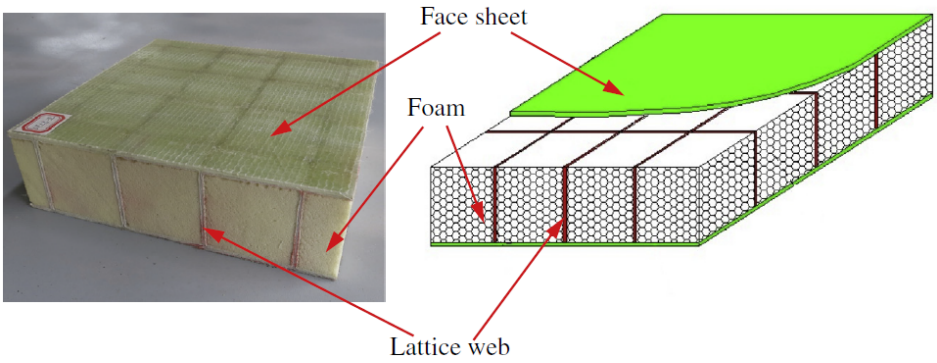


Figure 2.10: Foam filled composite sandwich structure [15]

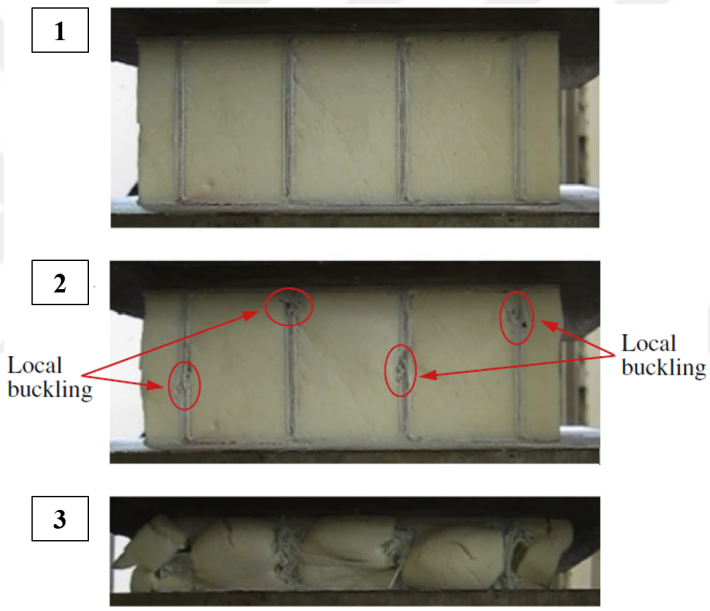


Figure 2.11: Compressive behaviour of foam filled structure with lattice web [15]

H. L. Fan et al. [16] proposed to use Kagome type carbon fibre reinforced lattice grids on core design. This is an optimized version of interlocked grid structures previously introduced by Han and Tsai. In this type of core design, fibres can be aligned in different directions on the unidirectional ribs so that their directions can be optimized to reach the most efficient material properties depending on the loading conditions. In Kagome type structure, ribs have three different orientations, which provides higher shear strength. On the other hand, there are only two rib crossings at the intersection points, which make interlocking process easier (see Figure 2.12).

After conducting experiments, Fan concluded that higher stiffness/strength than conventional core structures was obtained. However, the damage onset occurs at the adhesion region between the facesheet and the core in the form of debonding.

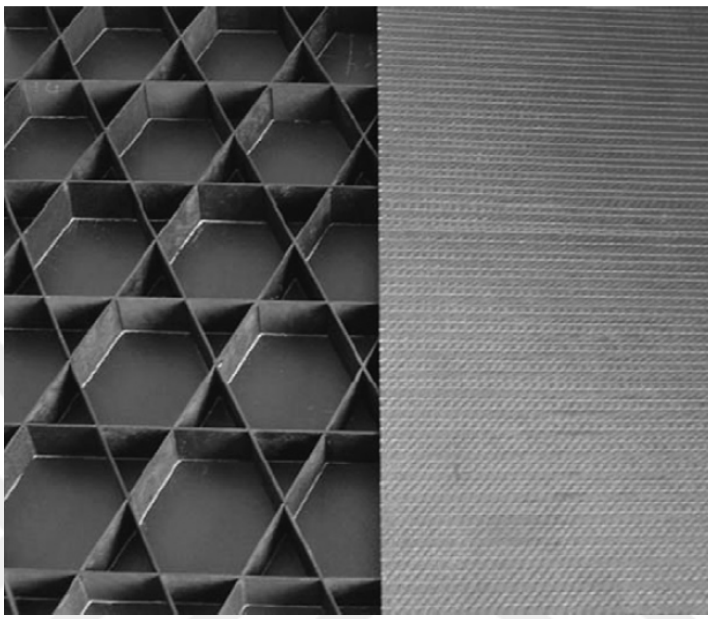


Figure 2.12: Sandwich panel with kagome lattice core [16]

Fengnian Jin et al. [17] proposed to use integrated woven cores to enhance facesheet-core debonding resistance. In this design, upper-lower facesheets and core were made of woven fabrics by a combination of body warp yarns and side weft yarns. All the areas where upper-lower facesheets were integrated by core are also woven by a co-shared weft yarn. Woven cores were aligned homogeneously in the length direction. This structure was subjected to in-plane compression, out-of-plane compression, shear and three point bending test. Figure 2.13 illustrates buckling failure of the structure under compressive load. Results showed that no debonding failure was observed and this structure exhibits higher facesheet-core debonding resistance compared to conventional core structures. However, out-of-plane compression and the shearing resistance in warp direction stood out as the main properties which must be improved.

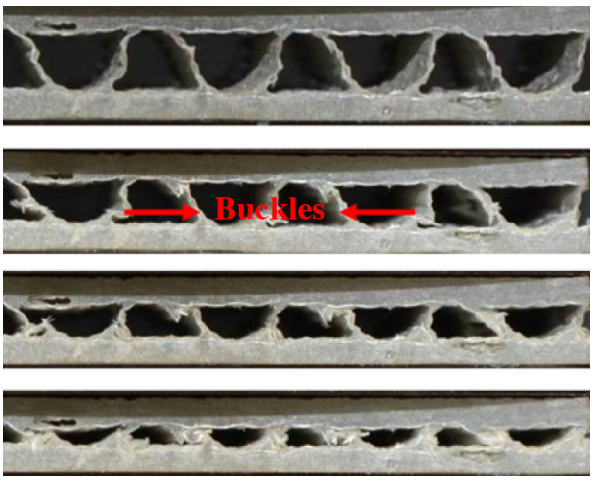


Figure 2.13: Buckling failure in woven core [17]

Hualin Fan et al. [18] proposed to use hierarchical pyramidal lattice truss core type in composite sandwich structures (see Figure 2.14). In this type, the core was made of glass fibre reinforced woven textile and it was manufactured by using interlocking method. The core part was designed so that overall structure exhibited better resistance to weft-loading conditions. Experimental results showed that it had better anti-crushing resistance than other integrated woven lattice sandwich composites (IWLSCs). Moreover, its specific energy absorption capacity was much higher than metallic lattice truss materials. However, buckling failure of rib made the structure brittle.

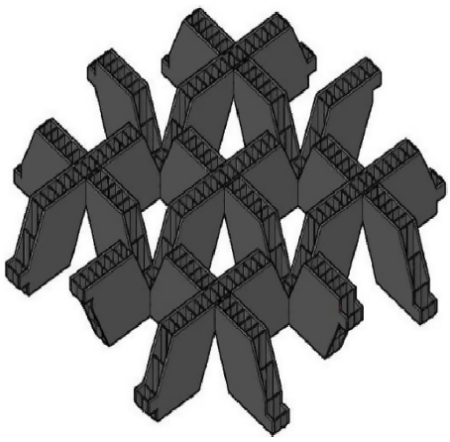


Figure 2.14: Pyramidal lattice truss panel [18]

Kenan et al. [19] claimed that the main drawback of existing sandwich structure designs was the debonding between core and facesheets. A new core design was proposed to improve this property by increasing adhering contact surface between core and facesheets. In his study, a novel processing method was adopted to eliminate secondary bonding operations by manufacturing the sandwich structure in a single process and two different lay-ups were investigated (see Figure 2.15). Load-carrying capacities and failure mechanisms were compared by performing three point bending tests. It was concluded that panels manufactured by using second lay-up method had more load-carrying capacity.

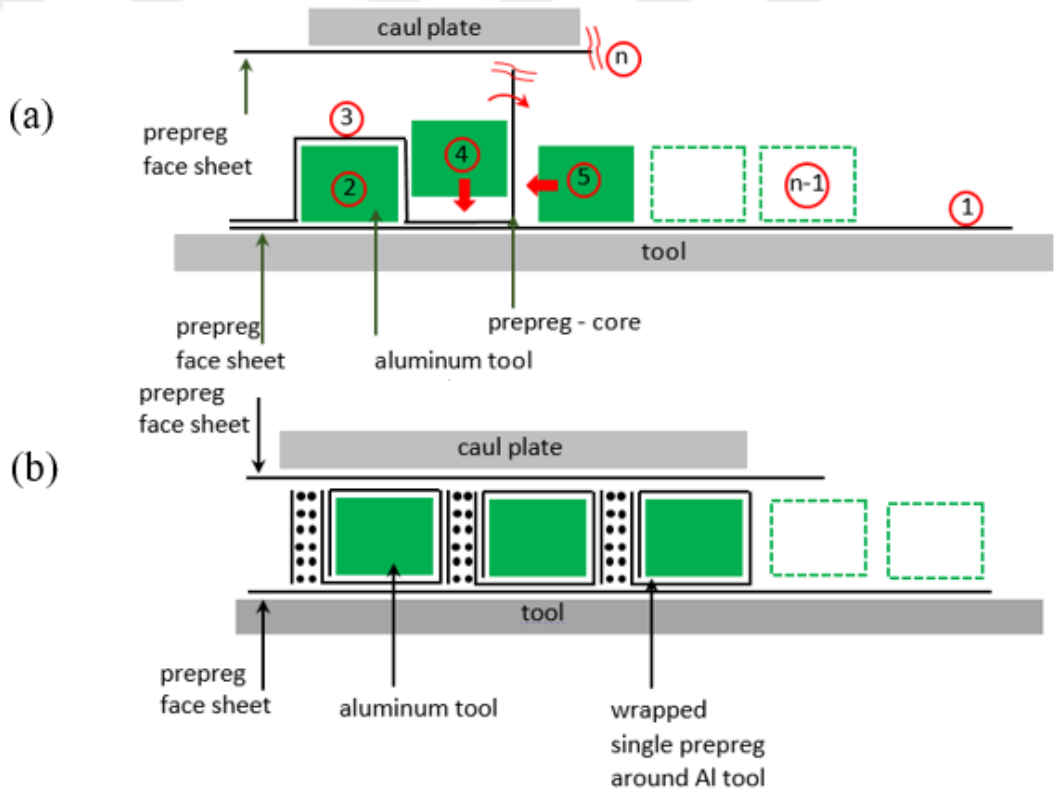


Figure 2.15: a) Schematic representation of the first lay-up method, b) Schematic representation of the second lay-up method [19]

2.2. Failure Modes

2.2.1. Failure Modes of Composite Materials

Failure modes of composite materials can be categorized as intralaminar and interlaminar failures. Intralaminar failure occurs inside the layer and it includes fibre tension failure modes (such as; fibre breaks, fibre pull-outs), fibre compressive failure modes (such as; fibre crushing, fibre kinking), matrix breaking, matrix crushing and fibre/matrix debonding. Schematic Figures 2.16, 2.17, 2.18 and 2.19 show the matrix and fibre failure modes at different loadings [20].



Figure 2.16: Fibre failure modes: (a) Shear fibre failure under compression load in fibre direction (b) Tensile fibre failure under tensile load in fibre direction [20]

As it is illustrated in Figure 2.16.(a), fibre compressive failure occurs due to shear behavior of matrix and defects in laminate such as voids and fibre misalignments. Fiber micro-buckling and formation of kinking bands are results of this failure mode. Figure 2.16.(b) shows the tensile failure in fibre direction. This failure occurs when fibre can not bear the applied load and it breaks in brittle behaviour at the weakest cross-section.



Figure 2.17: Matrix failure modes: (a) Shear matrix failure under compression load in transverse direction (b) Tensile matrix failure under tensile load in transverse direction [20]

Figure 2.17.(a) illustrates matrix failure under compression load in transverse direction. This failure mode occurs due to high shear stress in matrix material and the crack for this type of failure is most often at an angle to the loading direction. Figure 2.17.(b) exhibits tensile matrix failure and it occurs perpendicular to the applied tensile load in transverse direction.

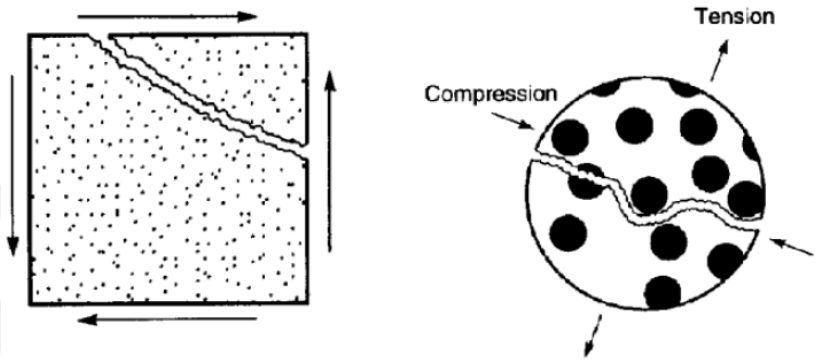


Figure 2.18: Shear failure in the 2-3 plane [20]

Figure 2.18 shows failures due to shear load in 2-3 plane. Since shear stress causes a tensile stress on the plane oriented 45°, shear load carrying capacity of material depends on matrix tensile strength, fiber tensile strength and matrix/fiber interfacial strength. Figure 2.19 shows failure in shear in 1-2 plane. It occurs due to separation of matrix from fibre along the length of the fibre and matrix interface.

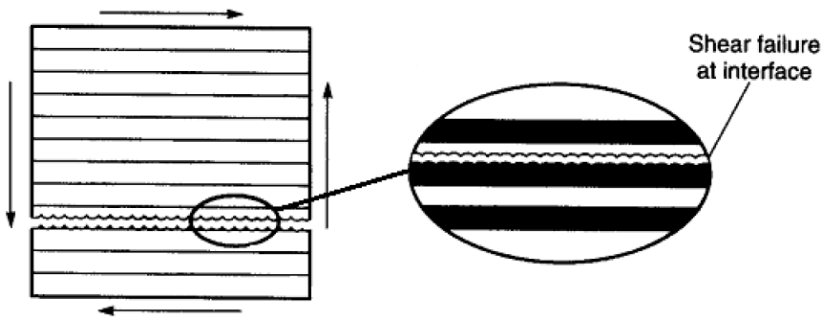


Figure 2.19: Failure in shear in the 1-2 plane [20]

Interlaminar failure refers to breaking down of cohesion force between adjacent layers, which can cause layers to separate. The interlaminar failure mode is also called as delamination (see Figure 2.20). It occurs mainly due to geometrical discontinuities such as matrix cracks and notches or manufacturing related defects. A delamination crack is often preceded by a crack which propagates through a ply until it has reached the fibres of an adjacent ply. Then, it starts to propagate along the interface between adjacent plies and results in delamination.



Figure 2.20: Delamination failure [21]

2.2.2. Failure Modes of Sandwich Structures

Failure modes of sandwich structures can be identified depending on geometry of sandwich structure, material properties, geometry of impact object and its velocity [22]. The main failure modes of sandwich structures are core crushing, delamination, fracture of facesheets, face wrinkling, buckling, shear crimping, facesheet-core debonding and core shear failure [23]. Typical failure modes of a sandwich structure are illustrated in Figure 2.21.

Core shear failure occurs when the principle stresses in the core section exceeds shear strength of core material. Local core crushing occurs due to excessive compressive point load when there is no reinforcement of facesheet or core in the load area.

Face wrinkling refers to local buckling of facesheet subjected to compression or bending. Facesheet compression fracture and global buckling may occur due to compressive loads in sandwich structure. Shear crimping refers to local buckling of the structure and it arises when the core thickness and shear modulus are not adequate enough to carry compressive loads.

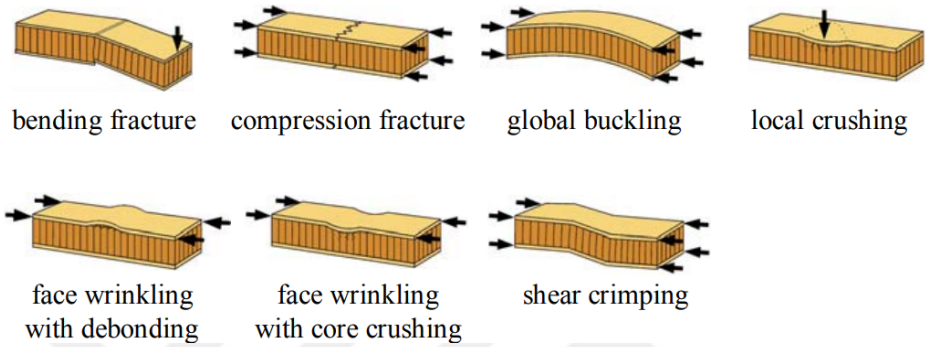


Figure 2.21: Sandwich structure failure modes [24]

2.3. Progressive Failure Analysis

A laminated composite structure might have different local failures at the same time under normal operating condition and might be still functional. More specifically, although a ply fails, it might still contribute stiffness and strength to the structure. Therefore, the composite structure might continue to carry load until all plies fail. It is essential to predict the initiation and propagation of such damages in order to develop safe and reliable composite structures. Therefore, using a solid failure analysis methodology is quite crucial. A typical progressive failure analysis method can be investigated in five basic steps [25]. Firstly, a load is applied and stress distribution on lamina is determined. Secondly, a failure criterion is used to check if there is any local lamina failure and to determine failure mode. If there is no failure, the load is increased until reaching any local failure. After failure is detected, new local material properties are determined by using material degradation rule and constitutive equilibrium equation is re-established. This procedure continues until the final failure.

There are some finite element programs to perform progressive failure analysis. In this study, ABAQUS software is used and three dimensional analysis is carried out. However, through-the-thickness in-ply failure behaviour is out of scope for this research because Hashin Failure Criterion is used to detect 2D in-ply failures. On the other hand, Cohesive Zone Model is defined to investigate delamination.

2.3.1. Intralaminar Failure Analysis

Fibre and matrix failures are the in-plane failure modes investigated under the scope of intralaminar failure analysis. Although it is impossible to detail each step of the intralaminar failure process, some theories are developed to predict in-plane failure response of a composite structure. Intralaminar failure analysis can be divided into two sub-steps: Damage initiation and damage evolution.

Figure 2.22 shows the stress-strain curve of a metal specimen obtained by a tensile test. The material response is assumed to be linearly elastic between points a-b. Then plastic deformation with strain hardening occurs, which is represented by curve b-c. Since CFRPs exhibit elastic-brittle behaviour, plastic deformation is not considered for composite materials. Therefore, curve a-c can be interpreted as linearly elastic for CFRPs. Point c identifies damage initiation and it is predicted by damage initiation criterion. On the other hand, c-d demonstrates stiffness degradation process and it is investigated by damage evolution law. The related elements are removed from analysis once the material stiffness is fully degraded at point d.

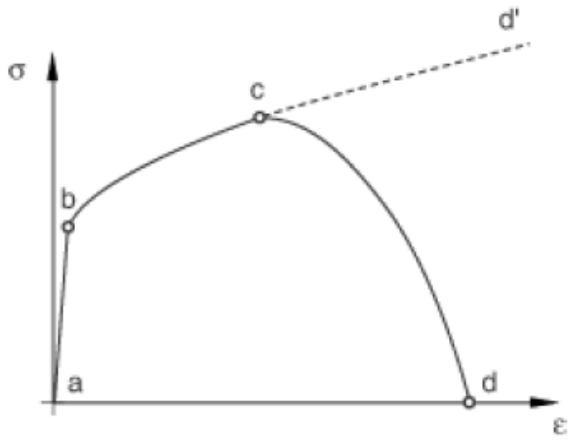


Figure 2.22: Typical stress-strain curve of a metal specimen [26]

2.3.1.1. Damage Initiation. There are mainly four major failure criteria widely used to predict the onset of in-ply damages for fibre-reinforced composite materials [27]: Maximum Stress, Tsai-Wu, Tsai-Hill and Hashin. Before explaining failure criteria in detail, it is important to define material coordinate system. As illustrated in Figure 2.23, direction–1 refers to fibre direction, direction–2 is transverse direction to fibre alignment and direction–3 represents through-the-thickness direction.

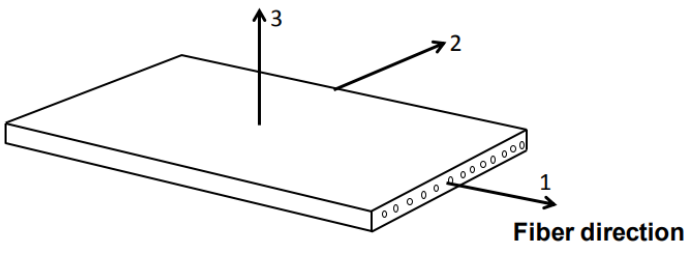


Figure 2.23: Material principal coordinate system

(I) Maximum Stress Criterion

This theory claims that failure occurs if one of the stress components in each orthogonal directions exceeds the corresponding allowable stress [20]. Maximum Stress Criterion is applied in the plane stress case and can not predict the through-the-thickness failures. In this theory, three different failure conditions are considered and they can be formulized as below:

- Fibre Failure: $\sigma_1^C > \sigma_1$ or $\sigma_1 > \sigma_1^T$
- Matrix Failure: $\sigma_2^C > \sigma_2$ or $\sigma_2 > \sigma_2^T$
- Shear Failure: $\tau_{12}^F > |\tau_{12}|$

Therefore, failure loads can be determined as:

$\sigma_1 = \sigma_1^C$, $\sigma_1 = \sigma_1^T$, $\sigma_2 = \sigma_2^C$, $\sigma_2 = \sigma_2^T$, $\tau_{12} = |\tau_{12}^F|$

where

σ_1: the nominal stress in fibre direction

σ_2: the nominal stress in transverse direction

τ_{12}: the nominal shear stress in plane–12

σ_1^T: the tensile strength in fibre direction

σ_1^C: the compressive strength in fibre direction

σ_2^T: the tensile strength in transverse direction

σ_2^C: the compressive strength in transverse direction

τ_{12}^F: the shear strength in plane–12

(II) Tsai-Wu Criterion

This origin of this theory is Von-Mises criterion for isotropic materials and it can be described as [20]:

$$\left(\frac{1}{2}\right)\left(\frac{1}{\sigma^Y}\right)^2 [(\sigma_1 - \sigma_2)^2 + (\sigma_1 - \sigma_3)^2 + (\sigma_2 - \sigma_3)^2] = 1 \tag{2.1}$$

where σ^Y is yield strength of the material. For orthotropic materials, this equation takes the form [20]:

$$F(\sigma_1 - \sigma_2)^2 + G(\sigma_1 - \sigma_3)^2 + H(\sigma_2 - \sigma_3)^2 + 2L\tau_{12}^2 + 2M\tau_{13}^2 + 2N\tau_{23}^2 = 1 \qquad (2.2)$$

where F, G, H, L, M and N are constants.
For the plane stress assumption, it can be re-described as:

$$F(\sigma_1, \sigma_2, \tau_{12}) = F_1\sigma_1 + F_2\sigma_2 + F_6\tau_{12} + F_{11}\sigma_1^2 + F_{22}\sigma_2^2 + F_{66}\tau_{12}^2 + 2F_{12}\sigma_1\sigma_2 + 2F_{16}\sigma_1\tau_{12} + 2F_{26}\sigma_2\tau_{12} \qquad (2.3)$$

where F_1, F_2, F_6, F_{11}, F_{22}, F_{66}, F_{12}, F_{16}, F_{26} are constants. The condition of no failure is given by:

$$F(\sigma_1, \sigma_2, \tau_{12}) < 1 \qquad (2.4)$$

All constants in this equation are determined by failure tests:
- By conducting uni-axial tension and uni-axial compression tests separately in direction–1, the material fails when $\sigma_1 = \sigma_1^T$ and when $\sigma_1 = \sigma_1^C$ respectively. Then;

$$F_1 = \frac{1}{\sigma_1^T} + \frac{1}{\sigma_1^C} \quad \text{and} \quad F_{11} = -\frac{1}{\sigma_1^T \sigma_1^C} \qquad (2.5)$$

- By conducting uni-axial tension and uni-axial compression tests separately in direction–2, the material fails when $\sigma_2 = \sigma_2^T$ and when $\sigma_2 = \sigma_2^C$ respectively. Then;

$$F_2 = \frac{2}{\sigma_2^T} + \frac{2}{\sigma_2^C} \quad \text{and} \quad F_{22} = -\frac{2}{\sigma_2^T \sigma_2^C} \qquad (2.6)$$

- By conducting pure shear test in plane–12, the material fails when $\tau_{12} = \tau_{12}^F$ or $\tau_{12} = -\tau_{12}^F$. Then;

$$F_6 = 0 \quad \text{and} \quad F_{66} = \left(\frac{1}{\tau_{12}^F}\right)^2 \qquad (2.7)$$

- By applying a known stress σ_1^* and applying shear stress τ_{12} until material fails, then;

$$F_{16} = 0 \quad \text{and} \quad F_{26} = 0 \tag{2.8}$$

- If Tsai-Wu is applied for the cases in which Von-Mises criterion is valid, it must give the same result as Von-Mises criterion. This is possible only if;

$$F_{12} = -\frac{1}{2}\sqrt{F_{11}F_{22}} \tag{2.9}$$

Finally all constants are known and the Tsai-Wu criterion is reduced to this form:

$$F_1\sigma_1 + F_2\sigma_2 + F_{11}\sigma_1^2 + F_{22}\sigma_2^2 + F_{66}\tau_{12}^2 - \sqrt{F_{11}F_{22}}\sigma_1\sigma_2 = 1 \tag{2.10}$$

(III) Tsai-Hill Criterion

This failure criterion is also an adopted version of Von-Mises criterion (Equation 2.1) in terms of laminates' failure modes [28]. In plane stress assumption, Von-Mises criterion reduces to:

$$\left(\frac{\sigma_1}{\sigma_Y}\right)^2 + \left(\frac{\sigma_2}{\sigma_Y}\right)^2 - \frac{\sigma_1\sigma_2}{\sigma_Y^2} = 1 \tag{2.11}$$

This criterion is modified to include composite materials' anisotropy so that it takes this form:

$$\left(\frac{\sigma_1}{\sigma_{1Y}}\right)^2 + \left(\frac{\sigma_2}{\sigma_{2Y}}\right)^2 - \frac{\sigma_1\sigma_2}{\sigma_{1Y}^2} - \frac{\sigma_1\sigma_2}{\sigma_{2Y}^2} + \frac{\sigma_1\sigma_2}{\sigma_{3Y}^2} + \left(\frac{\tau_{12}}{\tau_{12Y}}\right)^2 = 1 \tag{2.12}$$

By considering that composites are transversely isotropic and replacing metal yield stress with composite failure stress, final form of the Tsai-Hill criterion is obtained:

$$\left(\frac{\sigma_1}{\sigma_{1U}}\right)^2 + \left(\frac{\sigma_2}{\sigma_{2U}}\right)^2 - \frac{\sigma_1\sigma_2}{\sigma_{1U}^2} + \left(\frac{\tau_{12}}{\tau_{12}^F}\right)^2 = 1 \tag{2.13}$$

where σ_{1U} and σ_{2U} are compressive or tensile strength in direction–1 and direction–2 respectively.

(IV) Hashin Failure Criterion

Hashin Failure Criterion has the ability to predict four different failure modes of unidirectional lamina. These modes are tensile fibre failure, compressive fibre failure, tensile matrix failure, compressive matrix failure and can be formulized as below [27]:
- Tensile Fibre Failure Mode

$$\left(\frac{\sigma_1}{\sigma_1^T}\right)^2 + \left(\frac{\tau_{12}}{\tau_{12}^L}\right)^2 \geq 1 \tag{2.14}$$

- Compressive Fibre Failure Mode

$$\left(\frac{\sigma_1}{\sigma_1^C}\right)^2 \geq 1 \tag{2.15}$$

- Tensile Matrix Failure Mode

$$\left(\frac{\sigma_2}{\sigma_2^T}\right)^2 + \left(\frac{\tau_{12}}{\tau_{12}^L}\right)^2 \geq 1 \tag{2.16}$$

- Compressive Matrix Failure Mode

$$\left(\frac{\sigma_2}{2\tau_{12}^T}\right)^2 + \left[\left(\frac{\sigma_2^C}{2\tau_{12}^T}\right)^2 - 1\right]\frac{\sigma_2}{\sigma_2^C} + \left(\frac{\tau_{12}}{\tau_{12}^L}\right)^2 \geq 1 \tag{2.17}$$

where τ_{12}^L is the longitudinal shear strength and τ_{12}^T is the transverse shear strength in plane–12.

In ABAQUS software, in-ply damage initiation criterion for fibre-reinforced composites is based on Hashin's theory. For that reason, Hashin Failure Criterion is chosen for intralaminar failure analysis. As it is mentioned before, CFRPs shows no plastic deformation.

Therefore, the undamaged response of composite materials can be identified by orthotropic linear elasticity. Considering plane-stress case, since Hashin Failure Criterion is applicable only for 2D analysis, stress-strain relation can be defined as:

$$\begin{pmatrix} \epsilon_1 \\ \epsilon_2 \\ \gamma_{12} \end{pmatrix} = \begin{bmatrix} 1/E_1 & -\nu_{12}/E_1 & 0 \\ -\nu_{21}/E_2 & 1/E_2 & 0 \\ 0 & 0 & 1/G_{12} \end{bmatrix} \begin{pmatrix} \sigma_1 \\ \sigma_2 \\ \tau_{12} \end{pmatrix} \tag{2.18}$$

where ϵ_1, ϵ_2 and τ_{12} are normal strain in fiber direction, normal strain in transverse direction and shear strain in plane–12 respectively, E_1 and E_2 are Young's modulus in the fibre and transverse direction respectively, ν_{12} and ν_{21} are Poisson' ratios.
In ABAQUS, the damage onset based on Hashin's theory is expressed in the effective stress space [29]. The effective stress ($\hat{\sigma}$) is computed from:

$$\hat{\sigma} = M\sigma \tag{2.19}$$

where σ is the true stress and the damage operator (M) is:

$$M = \begin{bmatrix} \frac{1}{1-d_f} & 0 & 0 \\ 0 & \frac{1}{1-d_m} & 0 \\ 0 & 0 & \frac{1}{1-d_s} \end{bmatrix} \tag{2.20}$$

d_f, d_m and d_s represent current state of fibre damage, matrix damage and shear damage respectively. As indicated in Equation 2.21, 2.22 and 2.23, they are derived from damage variables, d_f^T, d_f^C, d_m^T, d_m^C corresponding to the four failure modes (tensile fibre, compressive fibre, tensile matrix, compressive matrix respectively) covered under the scope of Hashin Failure Criterion.

$$d_f = \begin{cases} d_f^T, & \text{if } \hat{\sigma}_{11} \geq 0 \\ d_f^C, & \text{if } \hat{\sigma}_{11} < 0 \end{cases} \tag{2.21}$$

$$d_m = \begin{cases} d_m^T, & \text{if } \hat{\sigma}_{22} \geq 0 \\ d_m^C, & \text{if } \hat{\sigma}_{22} < 0 \end{cases} \tag{2.22}$$

$$d_s = 1 - (1 - d_f^T)(1 - d_f^C)(1 - d_m^T)(1 - d_m^C) \tag{2.23}$$

Since there is no degradation prior to damage initiation, M is equal to identity matrix in the beginning. In other words, effective stress ($\hat{\sigma}$) is equal to true stress (σ). However, once damage initiation and evoluation occur for at least one failure mode, damage parameter (M) defined in Equation 2.20 is no longer an identity matrix and becomes a significant parameter in the criterion for damage initiations of other failure modes [30]. Since damage parameter (M) becomes bigger than unity, the effective stress representing stress level in the damaged area defined in Equation 2.19 increases, which has direct impact of damage initiation process of other modes. True stress tensor (σ) defined in Hashin Failure Criterion formulations is replaced with effective stress tensor ($\hat{\sigma}$).

2.3.1.2. Damage Evolution. For in-plane failure analysis, once damage initiation criterion reaches to the critical level according to Hashin's failure theory, the energy based damage evolution step begins. In damage evolution phase, the load-carrying capacity of composite structure dramatically reduces due to stiffness degradation. As illustrated in Figure 2.24, there is a sharp drop in load carrying capacity after damage initiation point A is reached. The path A-B represents damage evolution and the load carrying capacity continues declining until final failure point B is reached. At point B, stiffness matrix of the cohesive element is fully degraded and it no longer contributes any stiffness to the overall structure.

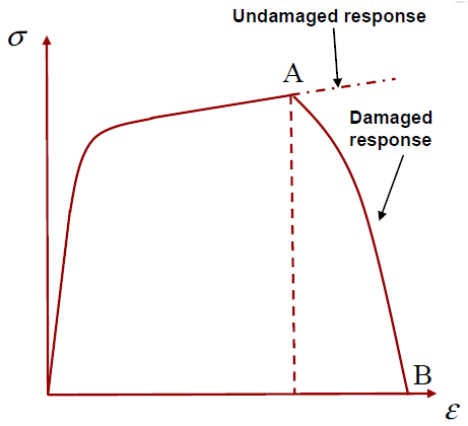


Figure 2.24: Typical material response showing progressive damage [26]

The damage evolution determines how the material reacts and at what rate the material stiffness degrades once the damage initiation criterion is satisfied. As it is indicated before, the material response is linearly elastic and represented by stiffness matrix of a 2-D orthotropic material before damage initiation. Therefore, the material behaviour is computed from [30]:

$$\sigma = C_d \epsilon \tag{2.24}$$

where C_d is the damaged elasticity matrix and ϵ is the strain. The damaged elasticity matrix is defined as:

$$C_D = \frac{1}{D} \begin{bmatrix} (1-d_f)E_1 & (1-d_f)(1-d_m)\nu_{21}E_1 & 0 \\ (1-d_f)(1-d_m)\nu_{12}E_2 & (1-d_m)E_2 & 0 \\ 0 & 0 & (1-d_s)GD \end{bmatrix} \tag{2.25}$$

where D=$1-(1-d_f)(1-d_m)\nu_{12}\nu_{21}$, G is the shear modulus, ν_{12} and ν_{21} are Poisson' ratios. As indicated in Damage Initiation Section, d_f, d_m, d_s reflects the current state of fiber damage, matrix damage, shear damage respectively and computed by using Equations 2.21, 2.22, 2.23. Damage variable parameters (d_i) are 0 in the beginning.

After damage initiation starts, these parameters are updated along with the damaged elasticity matrix. When a damage variable parameter reaches to unity at a certain load level, the related element no longer implements any stiffness and no longer carries load. This is where complete failure occurs for the related element.

ABAQUS introduces characteristic length (L^c) into formulation to reduce mesh dependency and to express the constitutive law as stress-displacement relation. Characteristic length depends on the element geometry and formulation. Figure 2.25 shows equivalent stress-displcement curve. Positive slope is determined by linear elastic material behaviour whereas negative slope after damage initiation is achieved by evolution of damage parameters based on equivalent stress and displacement equations for four different failure modes.

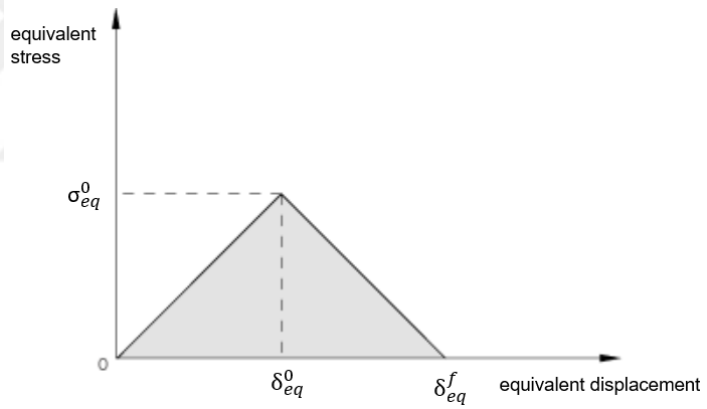


Figure 2.25: Equivalent stress-displacement curve [30]

- Tensile Fibre Failure Mode ($\hat{\sigma}_{11} \geq 0$)

$$\delta^{ft}_{eq} = L^c \sqrt{\langle \epsilon_{11} \rangle^2 + \alpha \epsilon^2_{12}} \tag{2.26}$$

$$\sigma^{ft}_{eq} = \frac{\langle \sigma_{11} \rangle \langle \epsilon_{11} \rangle + \alpha \tau_{12} \epsilon_{12}}{\delta^{ft}_{eq} / L^c} \tag{2.27}$$

- Compressive Fibre Failure Mode ($\hat{\sigma}_{11} < 0$)

$$\delta_{eq}^{fc} = L^c \langle -\epsilon_{11} \rangle \tag{2.28}$$

$$\sigma_{eq}^{fc} = \frac{\langle -\sigma_{11} \rangle \langle -\epsilon_{11} \rangle}{\delta_{eq}^{fc} / L^c} \tag{2.29}$$

- Tensile Matrix Failure Mode ($\hat{\sigma}_{22} \geq 0$)

$$\delta_{eq}^{mt} = L^c \sqrt{\langle \epsilon_{22} \rangle^2 + \epsilon_{12}^2} \tag{2.30}$$

$$\sigma_{eq}^{mt} = \frac{\langle \sigma_{22} \rangle \langle \epsilon_{22} \rangle + \tau_{12} \epsilon_{12}}{\delta_{eq}^{mt} / L^c} \tag{2.31}$$

- Compressive Matrix Failure Mode ($\hat{\sigma}_{22} < 0$)

$$\delta_{eq}^{mc} = L^c \sqrt{\langle -\epsilon_{22} \rangle^2 + \epsilon_{12}^2} \tag{2.32}$$

$$\sigma_{eq}^{mc} = \frac{\langle -\sigma_{22} \rangle \langle -\epsilon_{22} \rangle + \tau_{12} \epsilon_{12}}{\delta_{eq}^{mc} / L^c} \tag{2.33}$$

The area under σ_{eq}–δ_{eq} curve in Figure 2.25 represents the energy dissipated due to failure. In order to fully define stress-displacement curve for damage evolution process, fracture energy values must be given for each failure mode. The damage variable for a particular failure mode is determined by the following formula:

$$d = \frac{\delta_{eq}^{f} (\delta_{eq} - \delta_{eq}^{0})}{\delta_{eq} (\delta_{eq}^{f} - \delta_{eq}^{0})} \tag{2.34}$$

where δ_{eq}^{0} is the equivalent damage initiation displacement for the particular failure mode and δ_{eq}^{f} is the equivalent displacement at which complete failure occurs for that mode. Figure 2.26 shows how damage variable changes with respect to equivalent displacement.

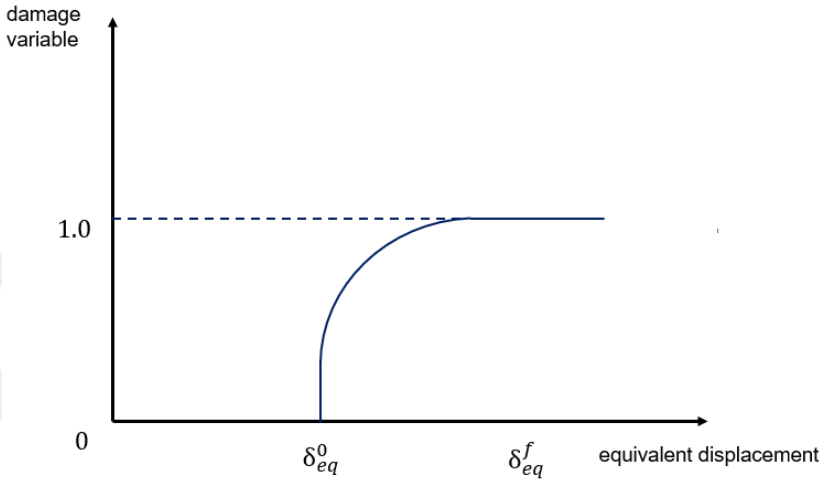


Figure 2.26: Damage variable as a function of equivalent displacement [30]

2.3.2. Interlaminar Failure Analysis

Delamination is a very common failure mode in the adhesively layered composites. This failure mode might arise as a result of weak surface bonding between different plies or geometrical discontinuities. In the adhesively layered composites, the structure's ability to carry load depends on bonding strength, which is a function of adhesive layer, adherents and their interfaces. In order to predict the behaviour of interfaces between adjacent plies in a composite structure, Cohesive Zone Model (CZM) must be defined.

CZM formulates the constitutive relation between traction forces on the bonding surfaces and interfacial separation of these surfaces. It helps to capture the crack initiation as well as crack propagation. Although this is a phenomenological approach and not directly related to the physical process in the damage zone, CZM is still a convenient tool for fracture predictions. It covers both of the strength-based approach and energy-based approach to fracture.

In CZM, the fracture mechanism is considered as a gradual process. The separation of cohesive surfaces ahead of the crack tip is resisted by cohesive traction. As the cohesive surfaces separate from each other, the traction between these surfaces increases firstly and reaches to a maximum. After a certain point, the cohesive traction starts losing its ability to keep surfaces together and then reduces to zero where separation process is completed. This process is formulized by using sets of equations such as traction-separation laws.

Although there are different forms of traction-separation law, the available version in ABAQUS software assumes initial linear elastic behaviour followed by initiation and evolution of the damage. For damage evolution step, linear and exponential softening laws are available in ABAQUS.

In this study, linear softening law is used for that phase. Therefore, the form of traction-separation law used to define CZM is bilinear as illustrated in Figure 2.27.

Figure 2.27 represents traction-separation law for pure modes used in the cohesive zone model [31]. It is defined by interlaminar properties such as interfacial normal strength (τ_n^o) and shear strength (τ_s^o, τ_t^o), normal penalty stiffness (K_n) and shear penalty stiffness (K_s, K_t), interfacial normal energy (G_n) and shear energy (G_s, G_t). Furthermore, (δ_n^o), (δ_s^o), (δ_t^o) represent corresponding initiation separations and (δ_n^f), (δ_s^f), (δ_t^f) represent corresponding failure separations. In this illustration, n represents normal direction (mode-1) whereas s and t represent two different shear directions (mode-2 and mode-3) as in Figure 2.28 [31].

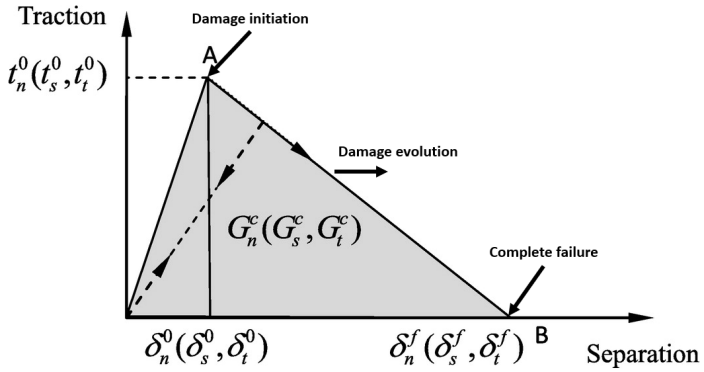


Figure 2.27: Bilinear form of traction-separation law [31]

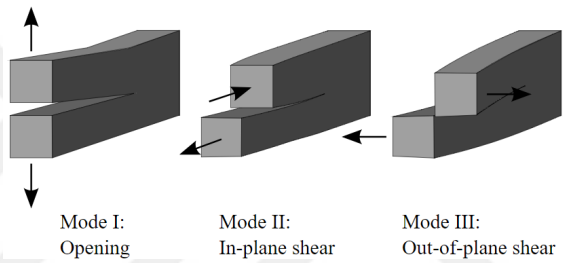


Figure 2.28: Failure modes [31]

As it is illustrated in Figure 2.27, the initial response of the material is based on Linear Elastic Fracture Mechanism (LEFM). In other words, the relation between traction strength and separation length of cohesive elements is assumed to be linear until crack initiation starts. The slope of this line refers to the penalty stiffness (K_i):

$$K_i = \frac{\tau_i^o}{\delta_i^o} \tag{2.35}$$

where $i = 1, 2, 3$ is fracture mode, τ_i^o is the critical mode strength and δ_i^o is the critical mode separation. Traction and separation increase linearly up to damage initiation point. There are four damage criteria for initiation of delamination [32]:

- Quadratic Stress Criterion

$$\left(\frac{\tau_n}{\tau_n^o}\right)^2 + \left(\frac{\tau_s}{\tau_s^o}\right)^2 + \left(\frac{\tau_t}{\tau_t^o}\right)^2 = 1 \tag{2.36}$$

- Maximum Stress Criterion

$$MAX\left\{\frac{\tau_n}{\tau_n^o}, \frac{\tau_s}{\tau_s^o}, \frac{\tau_t}{\tau_t^o}\right\} = 1 \tag{2.37}$$

- Quadratic Strain Criterion

$$\left(\frac{\delta_n}{\delta_n^o}\right)^2 + \left(\frac{\delta_s}{\delta_s^o}\right)^2 + \left(\frac{\delta_t}{\delta_t^o}\right)^2 = 1 \tag{2.38}$$

- Maximum Strain Criterion

$$MAX\left\{\frac{\delta_n}{\delta_n^o}, \frac{\delta_s}{\delta_s^o}, \frac{\delta_t}{\delta_t^o}\right\} = 1 \tag{2.39}$$

In this study, Quadratic Stress Criterion is used to predict initiation point of delamination damage. This criterion covers interaction between pure modes and provides more accurate failure prediction compared to other criteria [33]. In Quadratic Stress Criterion, damage evolution is modelled as a function of contact stress and overall damage at the contact point [32].

$$\tau_n = (1 - D)\overline{\tau}_n \tag{2.40}$$

$$\tau_s = (1 - D)\overline{\tau}_s \tag{2.41}$$

$$\tau_t = (1 - D)\overline{\tau}_t \tag{2.42}$$

where $\overline{\tau}_n$, $\overline{\tau}_s$, $\overline{\tau}_t$ represent the undamaged stress components at the contact point and they are predicted by traction-separation curve corresponding to current separation without any damage. D is the damage parameter and it represents overall damage at the contact point ranging from 0 to 1. When damage parameter becomes 1, the cohesive element at contact point reaches to final failure.

As it is indicated before, the traction-separation curve in Figure 2.27 is only for pure failure modes illustrated in Figure 2.28. However, in most cases, the structure is exposed to a combined loading condition. Therefore, the combination of several damage mechanisms acting simultaneously on the same material must be considered [32]. Figure 2.29 shows the mixed-mode response of cohesive interactions.

While the unshaded triangles in two vertical planes represent the material response under pure normal and shear loading, the intermediate shaded planes represent the material response under mixed-mode loading with different mode mixes.

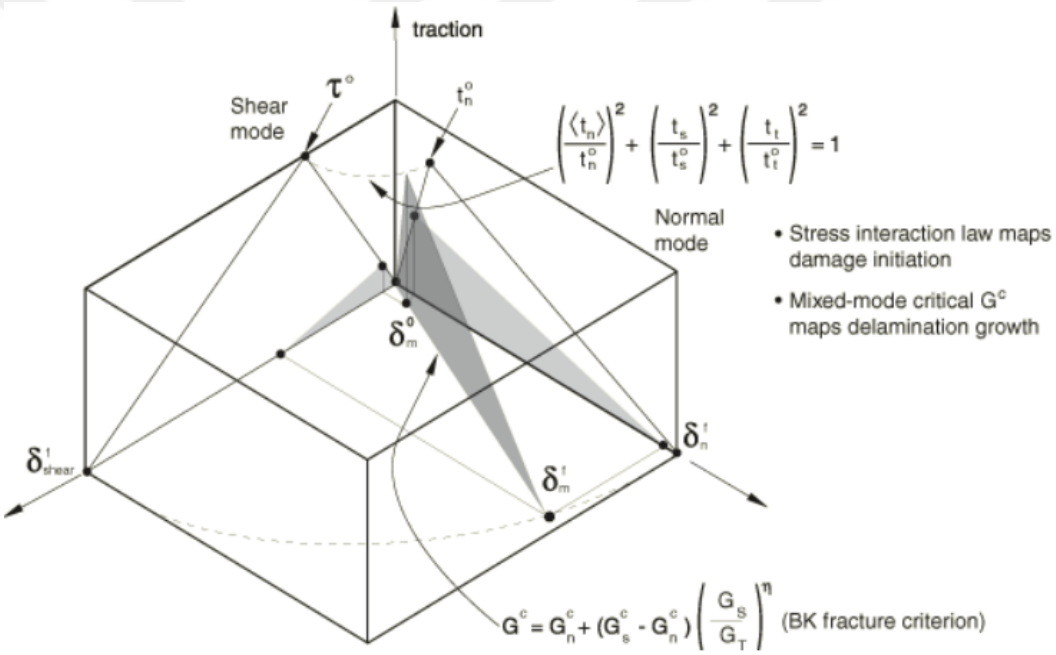


Figure 2.29: Mixed-mode response in cohesive interactions [32]

To evaluate a cohesive element under mixed-mode loading, effective displacement is introduced as:

$$\delta_m = \sqrt{\langle \delta_n^2 \rangle + \delta_s^2 + \delta_t^2} \tag{2.43}$$

Damage variable used in Equation 2.40, 2.41 and 2.42 is calculated as:

$$D = \frac{\delta_m^f(\delta_m^{max} - \delta_m^0)}{\delta_m^{max}(\delta_m^f - \delta_m^0)} \tag{2.44}$$

where δ_m^{max} refers to the maximum effective displacement obtained during loading history, δ_m^0 is the effective displacement at damage initiation and δ_m^f is the effective displacement at complete failure.

In this study, linear softening law is used together with mixed-mode fracture energy criterion. There are two energy criterion laws in ABAQUS software [32]: Benzeggagh-Kenane (BK) law and Power Law. Power law is defined in Equation 2.45.

$$\left(\frac{G_n}{G_n^c}\right)^\alpha + \left(\frac{G_s}{G_s^c}\right)^\alpha + \left(\frac{G_t}{G_t^c}\right)^\alpha = 1 \tag{2.45}$$

where G_n, G_s, G_t refer to the work done by the traction and its conjugate relative displacement in opening, in-plane, out-of-plane mode respectively and G_n^c, G_s^c, G_t^c refer to the critical fracture energies required to cause failure in opening, in-plane, out-of-plane mode respectively. BK law is applied when the critical fracture energies along first and second shear directions are the same (G_s^c=G_t^c) [34] and it is defined as follows 2.46.

$$G_n^c + (G_s^c - G_n^c)\left(\frac{G_S}{G_T}\right)^\eta = G^C \tag{2.46}$$

where

$$G^C = G_n + G_t + G_s \tag{2.47}$$

$$G_S = G_s + G_t \tag{2.48}$$

$$G_T = G_n + G_s \tag{2.49}$$

and η is a material property.

2.3.3. Modelling Progressive Failure Analysis in ABAQUS

In this section, FEA methods used to model composite structures are summarized. Especially, literature studies related with defining cohesive zone model and performing progressive failure analysis using ABAQUS software are explained. Furthermore, different approaches used to determine parameters required for a reliable FEA are compared to each other.

Sokolinsky et al. [35] perform finite elements analysis for crushing process of corrugated composite plate by using ABAQUS/Explicit and since its publication this study has been used as a benchmark to asses the success of progressive crushing of composite structures. Each ply is modelled separately by defining material properties, geometry and fibre orientation. Eight plies are bonded to each other (see Figure 2.30) and each one is meshed with continuum shell elements. Sokolinsky uses already implemented finite element code (Hashin Criterion) in ABAQUS to see in-plane damages of the structure. Cohesive Zone Model is defined by using General Contact option in ABAQUS/Explicit to investigate delamination failure. Generalized traction-separation law is used to define adhesive bonds between adjacent plies. The progression damage on the interface surfaces of adjacent plies is modelled by using mixed mode energy based on Benzeggagh-Kenane (BK) law. The load velocity is applied as 200 mm/sec to increase run time and it is indicated that dynamic effects are evident only beyond 500-1000 mm/sec. The simulation results are validated with experiments.

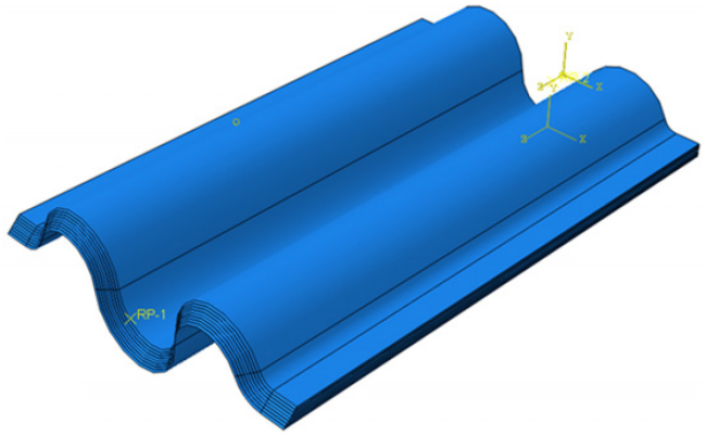


Figure 2.30: Sokolinsky corrugated composite model top view [35]

Turon et al. [36] investigate the parameters used in Cohesive Zone Models for composite structures. The choice of mesh size is quite crucial in FE simulations because it has direct impact on run time and analysis accuracy. More accurate results can be achieved with smaller mesh size but this might increase run time excessively. Therefore optimum mesh size must be chosen. This choice is made based on the number of elements in the cohesive zone. Turon defines the cohesive zone length as the distance from the crack tip to the point (see Figure 2.31) where the maximum cohesive traction is attained and formulates it as:

$$l_{cz} = E\frac{G}{(\tau^0)^2} \tag{2.50}$$

where E is Elastic Modulus, G is Interfacial Fracture Energy and τ^0 is Interfacial Fracture Strength. The number of elements in the cohesive zone is obtained with the equation:

$$N_e = \frac{l_{cz}}{l_e} \tag{2.51}$$

where l_e is the mesh size. The mesh size is adjusted by keeping the number of elements in a certain interval. Having too few elements in the cohesive zone might not capture the actual behaviour of delamination.

Therefore, it is crucial to meet the requirement of minimum number of elements in the cohesive zone. Moes et al. [37] suggest to use more than 10 elements in cohesive length whereas Falk et al. [38] use between 2 and 5 elements in their studies.

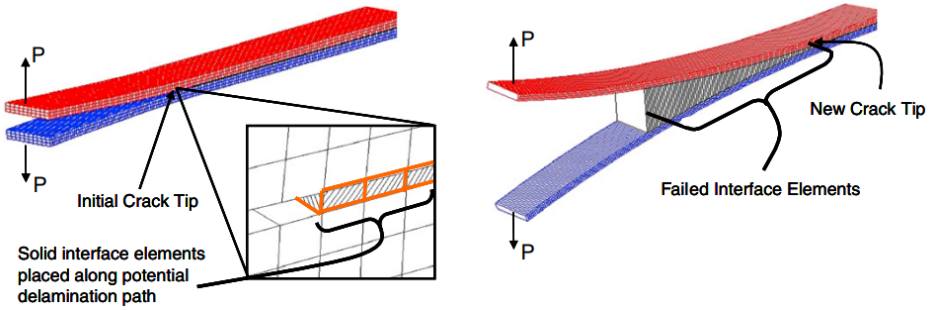


Figure 2.31: Cohesive zone elements and delamination in DCB [39]

Moslemi et al. [40] investigate the impact of mesh refinement on the simulation accuracy. Double Cantilever Beam (DCB) test is performed and the results are compared with DCB simulations. The cohesive element length ranges from 0.125 mm to 2 mm in DCB models while the cohesive zone length is determined as 3.76 mm. It is concluded that cohesive element length smaller than 1 mm is enough to get accurate results (see Figure 2.32). In other words, at least 3 elements are required in the cohesive zone to predict delamination behaviour accurately.

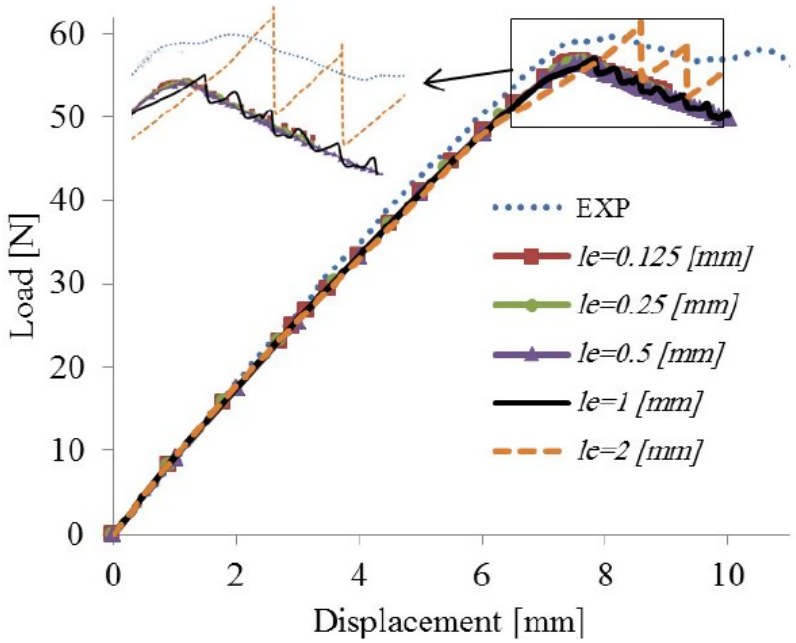


Figure 2.32: The effect of different element lengths on damage simulation [40]

Turon et al. [36] suggest that by keeping interfacial fracture energy constant and changing the interfacial fracture strength, the cohesive zone length can be increased artificially, which means that larger elements can be used to apply the Falk's recommendation to use 2-5 elements over the cohesive zone length. By implementing Equation 2.51 into Equation 2.50, the artificial interfacial fracture strength can be formulized as:

$$\overline{\tau}^{o} = \sqrt{\frac{EG}{N_e l_e}} \tag{2.52}$$

where $\overline{\tau}^{o}$ represents adjusted interfacial fracture strength. In order to reduce the computational time without sacrificing accuracy of the results, the interfacial fracture strength needs to be artificially reduced by using Equation 2.52. Figure 2.33 shows accuracy of Turon's approach. During mesh convergence process, interfacial fracture strength is reduced according to Equation 2.52 while implementing different mesh sizes, while keeping the minimum number of elements in cohesive zone length as 5. It is concluded that accurate results are obtained with this approach for mesh size smaller than 2.5 mm

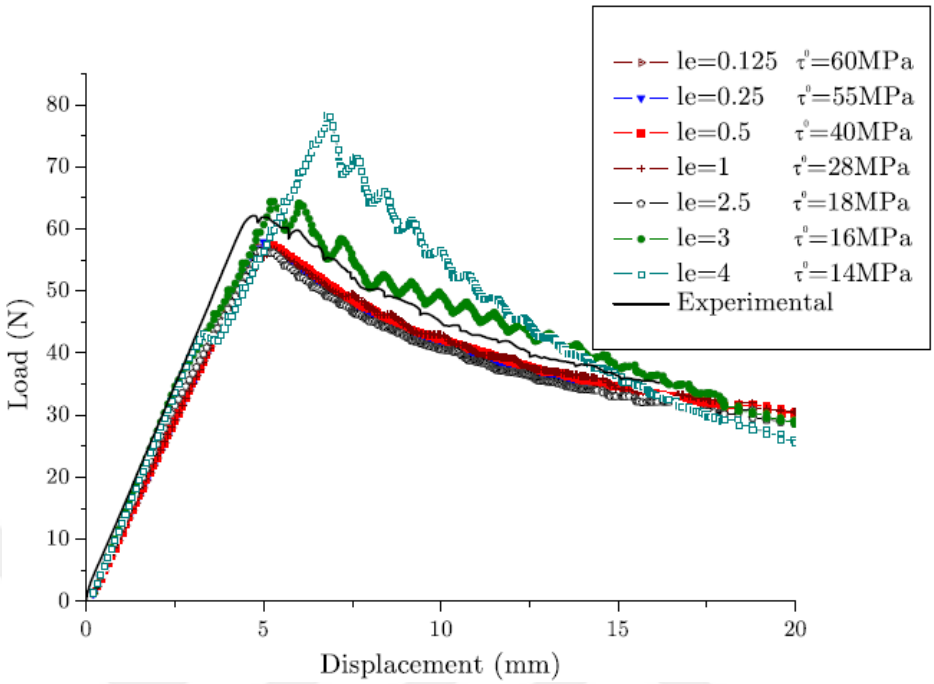


Figure 2.33: The effect of artificial interfacial fracture strength [36]

Penalty stiffness shows the linear relationship between traction strength and separation length of cohesive elements. There are different approaches in literature to determine penalty stiffness values of cohesive elements. Zou et al. [41] claim that penalty stiffness must be between 10^4 and 10^7 times the interfacial strength per length. Camanho et al. [42] achieve accurate predictions by using value of 10^6 N/mm^3 for penalty stiffness. Turon et al. [43] claim that the effective elastic properties of the material are not affected by the cohesive surface as long as the through-the-thickness Young's modulus of the material (E_3) is much less than multiplication of the lamina thickness (t) and penalty stiffness (K). It is concluded that penalty stiffness can be formulized as:

$$K_i = \beta \frac{E_i}{t} \tag{2.53}$$

where β is a parameter larger than 1. It is recommended to choose β as 50. DCB test is conducted and FEA is performed with different penalty stiffness values to see its effect on simulation accuracy and run time.

It is concluded that the load-displacement curves with stiffness values greater than 10^4 N/mm^3 are adequately close to test results and simulations with stiffness values less than 10^4 N/mm^3 are not efficient to capture actual load-displacement curve. On the other hand, the number of iterations required for solution with stiffness values less than 10^4 N/mm^3 is much greater than the number of iterations required for solution with stiffness values higher than 10^4 N/mm^3. Figure 2.34 shows the effect of penalty stiffness on simulation accuracy and number of iterations. The stiffness value calculated by Equation 2.53 is 5.55×10^5 N/mm^3. It is concluded that Turon's approach gives the ideal stiffness value in terms of simulation accuracy and run time. In this study, penalty stiffness values are calculated by using Equation 2.53 and suggested β value by Turon.

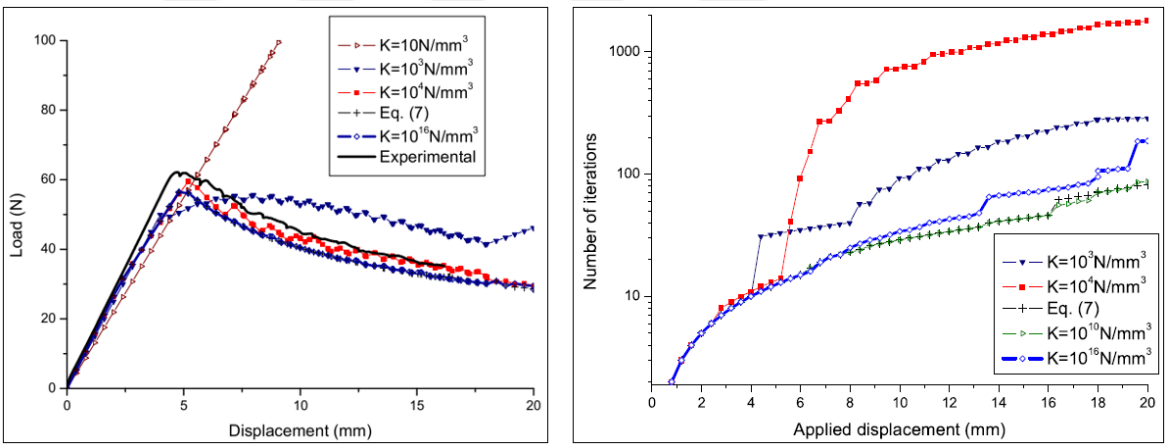


Figure 2.34: The effect of penalty stiffness on simulation accuracy and number of iterations [43]

Chen et al. [44] work on an approach to predict the delamination behaviour of a composite T-piece structure by using ABAQUS. In this study, different energy criterion laws, Power Law and Benzeggagh-Kenane (BK), available in ABAQUS software are compared to each other in terms of their ability to agree with actual test results. The linear softening damage criterion is used with BK law where $\alpha = 1$ or 2 and with Power Law where $\alpha = 1$ or 2. The effect of these different energy criterion laws and α values on the delamination prediction is investigated by comparing simulation results with test results.

As it is illustrated in Figure 2.35, BK law with $\alpha = 2$ gives the closest prediction to test results.

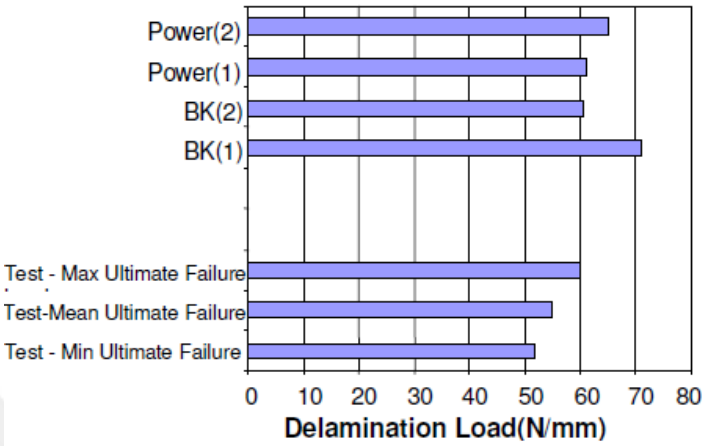


Figure 2.35: Comparison between prediction and test results [44]

2.4. Objectives

In this study, the progressive failure behaviour of a corrugated core type sandwich structure is analyzed by both numerical and experimental methods. The core design proposed by Kenan et al. [19] is chosen as specimen geometry. In this sandwich structure, contact surface between core and facesheets is higher compared to counterpart designs and this is the main advantage in terms of avoiding debonding failure [19]. The main aim of this thesis is to investigate failure behaviour of this special composite sandwich structure. Compression and four-point bending tests are performed as well as a finite element model is developed to predict the failure behavior of the specimens under the loading conditions in these tests. Hashin Failure Criterion is implemented to predict in-ply failures and Cohesive Zone Model is defined to simulate delamination behaviour. Finally, progressive failure analysis and experimental results are compared and the accuracy of FEA is discussed.

3. NUMERICAL ANALYSIS

Commercial finite element program ABAQUS/Explicit is used to simulate the behaviour of corrugated core type composite sandwich structure under quasi-static loading condition. Although implicit solver seems to be appropriate choice for quasi-static analysis, it is recommended that explicit solver is more efficient especially for simulations involving contact and large deformations [45].

First of all, the solid model of each ply is created separately as three dimensional extrusions. This allows the user to define material, fibre direction, ply thickness and geometry unique to each ply. In the modelled structure, the stacking sequence is [90/0/90/0] for upper/bottom facesheets and [0/90/0/90] for webs. Each ply thickness is 0.184 mm. These parameters are defined for each ply by using "Composite Layup" option. Cross sections of Four-Point Bending Test Model and Compression Test Model are shown in Figures 3.1 and 3.2 respectively.

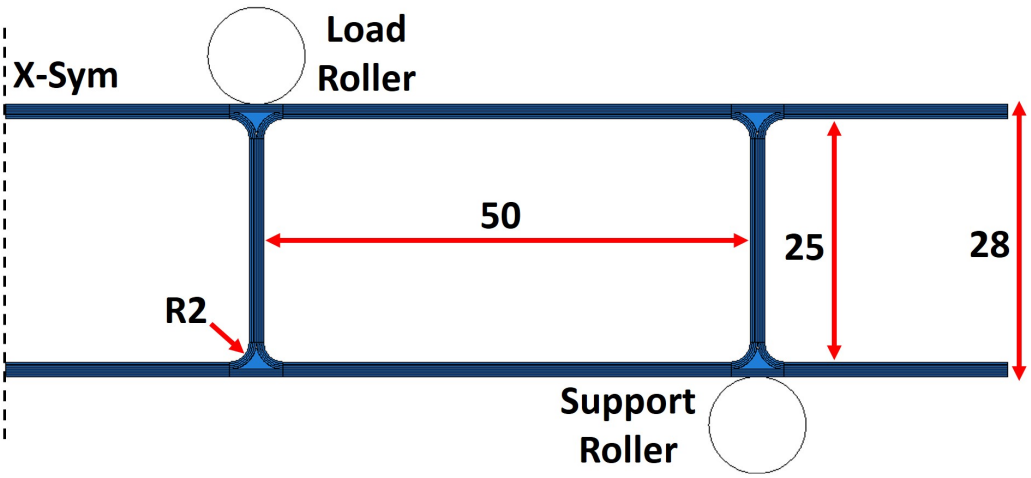


Figure 3.1: Cross section of four-point bending test model

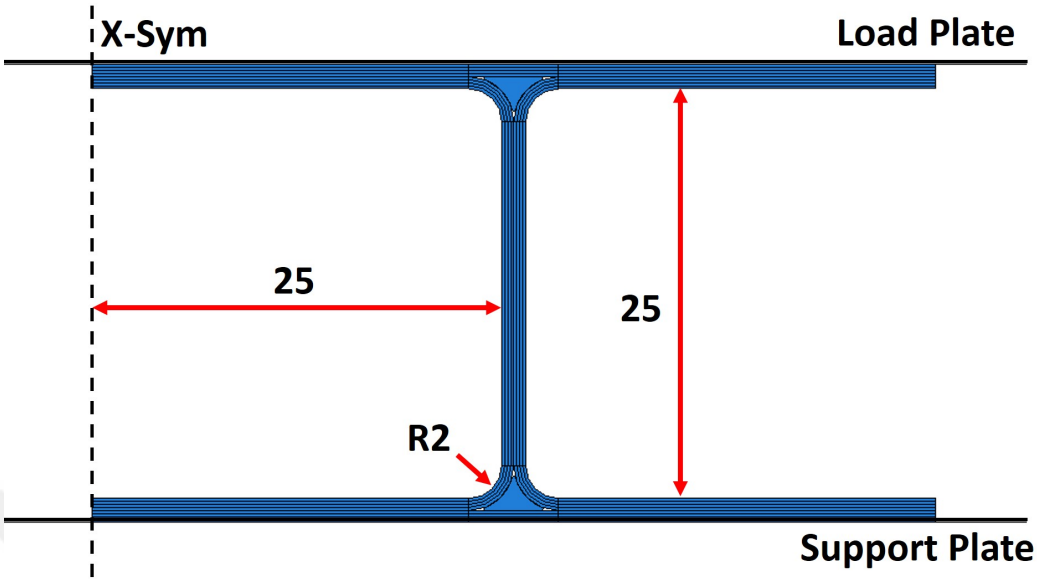


Figure 3.2: Cross section of compression test model

AS4/8552 material (carbon/epoxy prepreg) is used to manufacture the corrugated sandwich panels. Table 3.1 shows the material properties. Elastic material properties are defined in "Material" option. Hashin Damage Criterion is also defined in this option. It is a built-in tool in ABAQUS and it is fully defined by entering material allowable tensile, compressive, shear strength as well as tensile and compressive fracture energy.

After all parts representing each ply are fully defined, they are bonded to each other in "Assembly" module so that final shape of the sandwich structure is created. However, these plies are not numerically connected to each other yet. In "Interaction Properties" module, the contact properties of interaction surface between adjacent plies are defined. This is where CZM is also defined to perform interlaminar analysis and to investigate delamination behaviour of the structure.

Table 3.1: Material properties of AS4/8552 [46]

	SYMBOL	**VALUE**	**UNIT**
Cured Ply Nominal Thickness	t	0.184	mm
Nominal Laminate Density	ρ	1.58	gr/cm^3
Longitudinal Elastic Modulus	E_1	141	GPa
Transverse Elastic Modulus	$E_2 = E_3$	10	GPa
Shear Modulus in 1-2 Plane	$G_{12} = G_{13}$	5571	MPa
Shear Modulus in 2-3 Plane	G_{23}	3278	MPa
Poisson's Ratio	$\nu_{12} = \nu_{13}$	0.263	-
Longitudinal Tensile Strength	X_T	2207	MPa
Longitudinal Compressive Strength	X_C	1500	MPa
Transverse Tensile Strength	Y_T	81	MPa
Transverse Compressive Strength	Y_C	267	MPa
In-Plane Shear Strength	S	80	MPa

The penalty stiffness values are calculated for each mode by using Equation 2.53 recommended by Turon [36] and summarized in Table 3.2. These values are defined under "Cohesive Behaviour" option in "Interaction Properties" module. In order to fully define traction-separation curve, interfacial fracture strength and interfacial fracture energy parameters must be also introduced under "Damage Option". Interfacial fracture energy values for AS4/8552 prepreg material are determined by performing Double Cantilever Beam (DCB) test for Mode 1, End Notched Flexure (ENF) test for Mode 2 and the parameters for Mode 3 fracture are taken to be the same as Mode 2. The average fracture energy values for each failure mode are summarized in Table 3.2. Sina et al. [47] carried out DCB and ENF tests to determine interfacial fracture energy values for AS4/8552 and these parameters are used in this study. The related interfacial fracture strength values are adjusted by using Equation 2.52 and keeping the largest element length used in the model as 0.7 mm. Sina et al. [48] performed a mesh convergence study to reduce computation cost without sacrificing accurate prediction. It is found out that FEA results are reasonably close to test results as long as the largest element size used in FE model is equal to or smaller than 1 mm.

As it is indicated before, Falk et al. [38] suggest that implementing 2-5 elements in the cohesive zone length would give satisfying results. In this study, the number of element in the cohesive zone length is taken as 4, so the cohesive zone length is needed to be 2.8 mm. The interfacial fracture strength values adjusted per Equation 2.52 are also summarized in Table 3.2. The frictional force between the seperated surface is modelled under "Tangential Behaviour" option by defining friction coefficent. Friction coefficient are generally determined by experimental studies. In this study, it is chosen as 0.3 as indicated in Sokolinsky et al. [35].

Table 3.2: Interlaminar properties of AS4/8552

	SYMBOL	**MODE-1**	**MODE-2**	**MODE-3**	**UNIT**
Penalty Stiffness	$K_{n,s,t}$	$2.65x10^6$	$1.42x10^6$	$1.42x10^6$	N/mm^3
Interfacial Strength	$\tau^o_{n,s,t}$	35	70	70	MPa
Fracture Energy	$G_{n,s,t}$	0.28	2.59	2.59	KJ/m^2

Two different structures are modelled depending on core cell numbers. Boundary conditions are assigned as indicated in Figure 3.3 and 3.4. Constant velocity (300 mm/s) is defined to reference point of loading plate in compression model and reference point of loading roller in four-point bending model. Although implemented velocity is ten times higher than quasi-static test speed, increasing velocity is necessary to decrease run time for explicit analysis. Since dynamic effects become significant only beyond 500-1000 mm/s, the artificial increase in the velocity does not have an impact on numerical accuracy [35]. Both structure is modelled as half-section by using symmetry boundary condition in order to decrease run time. Compression model is supported by fixed bottom plate whereas four-point bending model is supported by fixed bottom roller. All nodes are fixed in z-direction to prevent unrealistic deformation behaviour. All plies except deltoid section are meshed with Continuum Shell Elements (SC8R). This element type has 3D geometry but its kinematic and constitutive behaviour are similar to those of conventional shell elements. In ABAQUS, built-in Hashin Failure Criterion is defined with Continuum Shell Element.

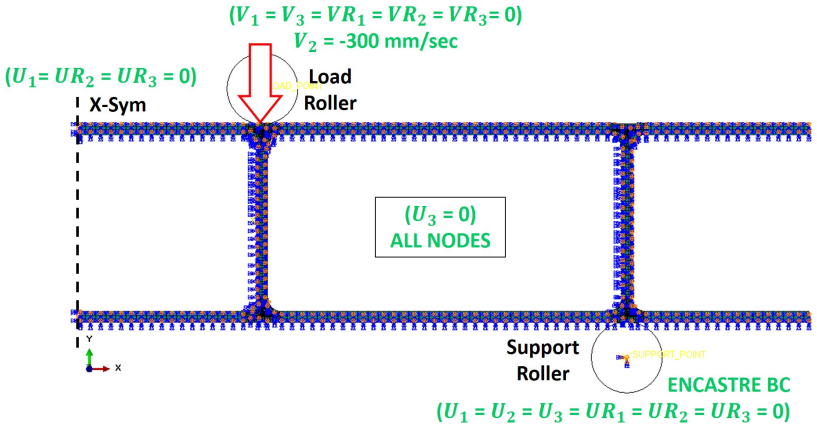


Figure 3.3: Boundary conditions of four-point bending test model

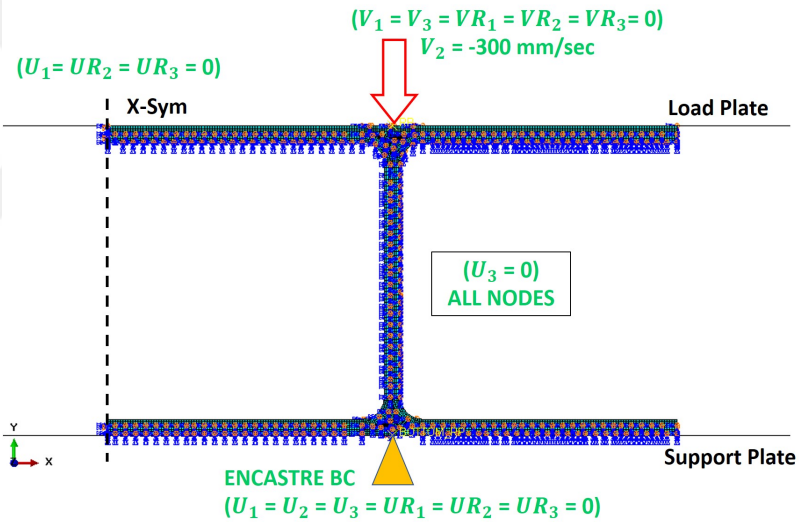


Figure 3.4: Boundary conditions of compression test model

One particular complication arises in the model due to the deltoid in the junction of the facesheets and the webs of the composite structure, as shown in Figure 3.5. This deltoid is formed during manufacturing by resin percolating into the pockets present in the preform. Those deltoids are modelled by solid elements. Since Hashin Criterion is not defined for solid elements in ABAQUS, failure within those deltoid sections can not be predicted. However, same type of Cohesive Zone Interaction is defined between the deltoids and adjacent plies, which enables the model to capture the separation of the adjacent plies from the deltoid.

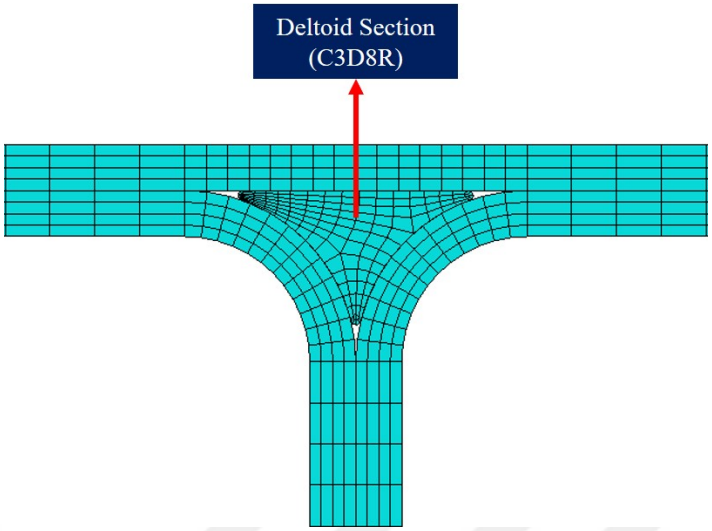


Figure 3.5: Deltoid section

4. EXPERIMENTAL STUDY

In the experimental study, compression test is carried out on the corrugated sandwich structure with one core cell whereas four-point bending test is performed on the structure with three core cells. The main purpose of the experiments is to investigate actual failure response of the corrugated core sandwich structures under quasi-static loading condition and obtain load-displacement curve to validate FEA results.

4.1. Specimen Preparation

Hexcel's unidirectional AS4/8552 prepreg system is used in this study [46]. Nominal thickness of this prepreg is 0.184 mm. First of all, a large corrugated plate is manufactured as follow: First, AS4/8552 prepregs are wrapped around nine aluminium mandrels, having 50 mm width and 25 mm thickness, with desired stacking sequence; [90/0/90/0]. These form the core sections. Then these wrapped nine mandrels are stacked horizontally next to each other. Afterwards facesheets are stacked on and under the aluminium mandrels with [0/90/0/90] lay-up orientation. Figure 4.1 shows schematic representation of stacking sequence and structure. Stacked plies with wrapped mandrels are placed under vacuum bag carefully. Then it is cured in autoclave according to the Manufacturer's Recommended Cure Cycle (MRCC) as shown in Figure 4.2. 7 bar pressure and -1 bar vacuum is applied during curing process to evacuate the air inside the prepregs. After curing, aluminium mandrels are removed easily thanks to the difference in thermal expansion coefficients of composite and aluminium materials.

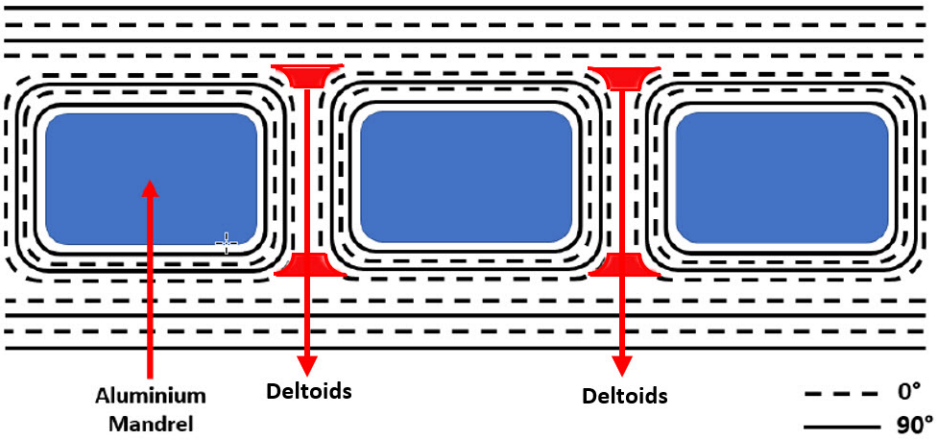


Figure 4.1: Schematic representation of lay-up

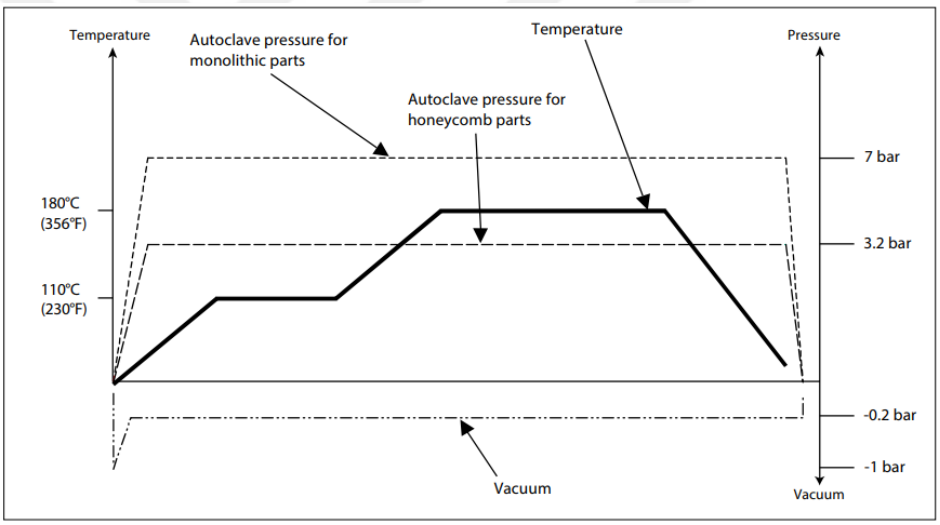


Figure 4.2: Curing cycle for AS4/8552 [46]

Test specimens are cut from the large corrugated plate using a water cooled diamond disc. Two specimens with one core section are cut for compression tests as shown in Figure 4.3. Moreover, two specimens with three core sections are cut for four-point bending tests as shown in Figure 4.4.

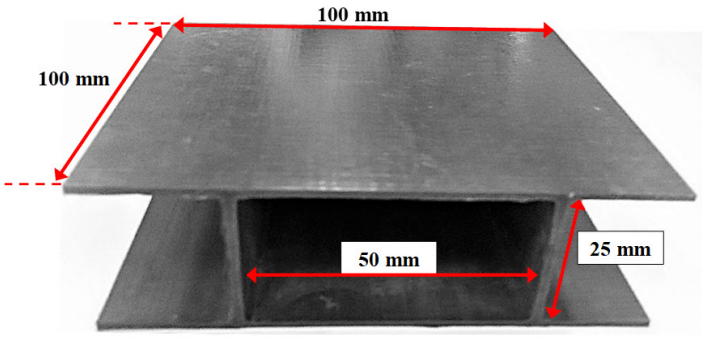


Figure 4.3: Compression test sample (dimensions in mm)

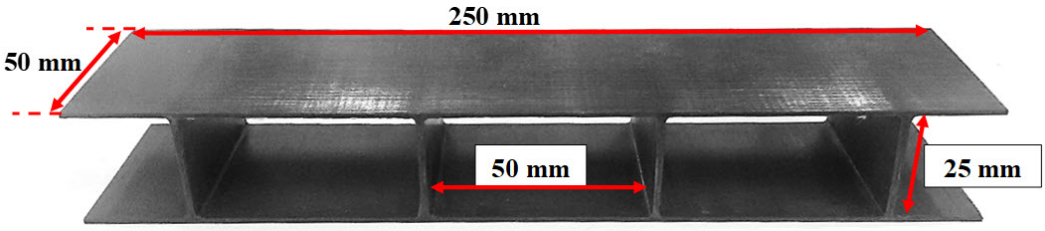


Figure 4.4: Four-point bending test sample (dimensions in mm)

4.2. Test Procedure

The compression test specimens are placed in horizontal position on a steel plate as shown in Figure 4.5. Load plate moves downward at 1 mm/min and compress the specimen until the total deformation reaches to 2 mm. Tests are stopped when the deflection reaches to 2 mm, since it is the level where the specimens cannot sustain load any more.

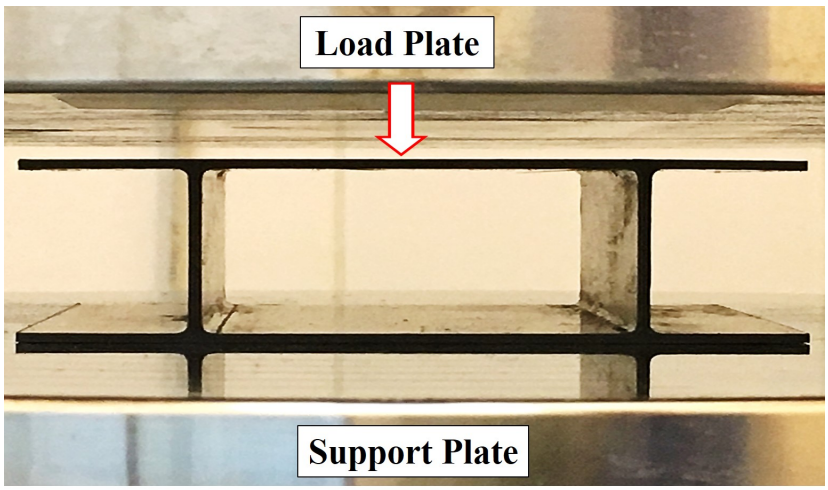


Figure 4.5: Compression test setup

Four-point bending test is performed for two specimens having three core sections. The specimens are supported by two rollers at right and left edges of the plate so that support rollers align vertically with outermost core ribs. Other two load rollers are aligned with inner core ribs from top of the structure and they move downward at 10 mm/min until total displacement of load rollers reaches to 30 mm. Figure 4.6 shows four-point bending experimental setup.

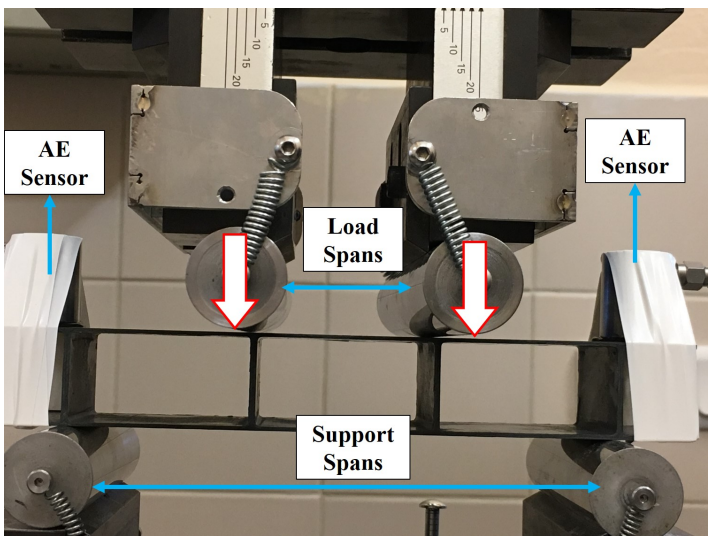


Figure 4.6: Four-point bending test setup

5. RESULTS AND DISCUSSION

5.1. Compression Test and FEA

Failure mechanisms observed during 1st compression test are illustrated in sequence in Figure 5.1. Firstly, buckling failure occurs in the middle of left rib section at a displacement of 0.49 mm. This is where first major load drop is seen. Then delamination initiates at this buckle zone at a displacement of 0.53 mm along with fibre breaks in 90° plies and matrix cracks in 0° plies. At the same displacement level, buckling starts also in the middle of right rib section. This is where second major load drop is seen. Then delamination initiates at this buckle zone in the right rib at a displacement of 0.55 mm along with fibre breaks in 90° plies and matrix cracks in 0° plies. Propagation of all delaminations, fibre breaks and matrix cracks continues by the end of test as seen in Figure 5.1.

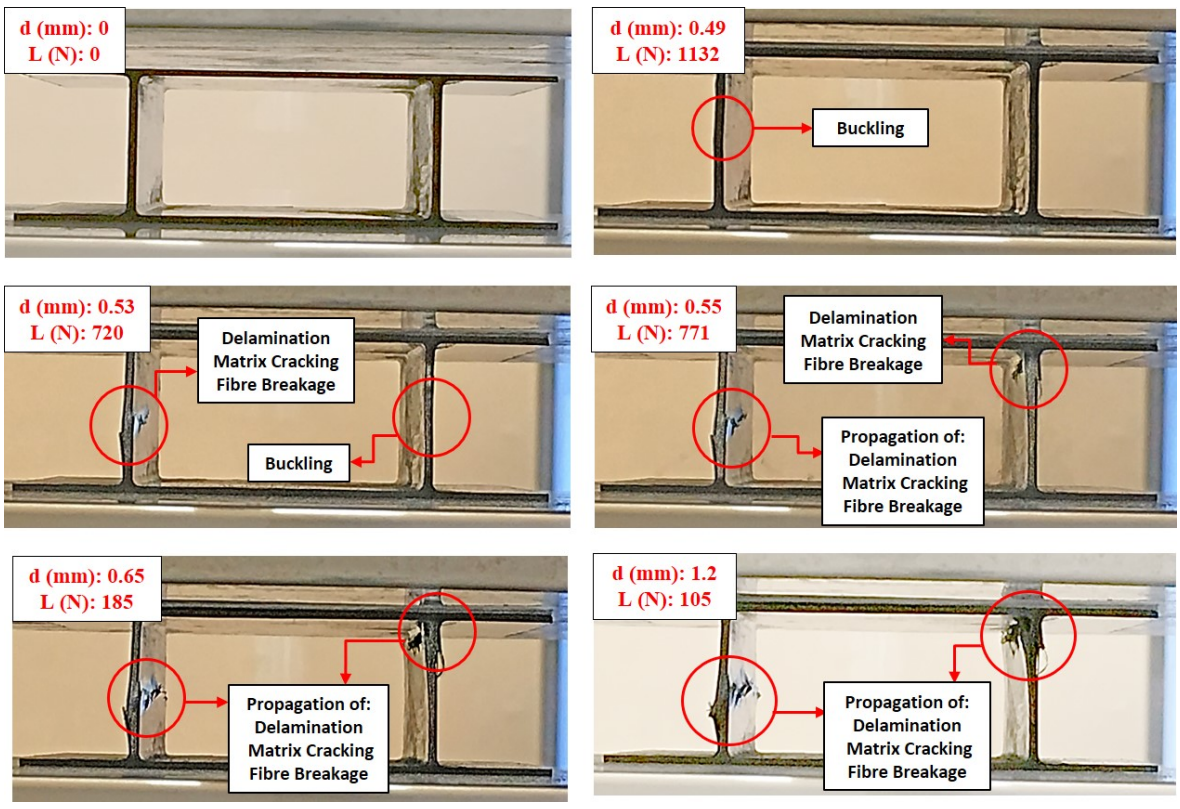


Figure 5.1: Failures in 1st compression test

Failure modes during the 2nd compression test are shown in Figure 5.2. It is observed that failure patterns are very similar to the 1st compression test. Buckling failure occurs in the middle of left rib section at a displacement of 0.52 mm. This is where first major load drop is seen. Then delamination initiates at this buckle zone at a displacement of 0.55 mm along with fibre breaks in 90° plies and matrix cracks in 0° plies. At the same displacement level, buckling starts also in the middle of right rib section. This is where second major load drop is seen. Then delamination initiates at the buckle zone in the right rib at a displacement of 0.58 mm along with fibre breaks in 90° plies and matrix cracks in 0° plies. Propagation of all delaminations, fibre breaks and matrix cracks continues by the end of test as seen in Figure 5.2.

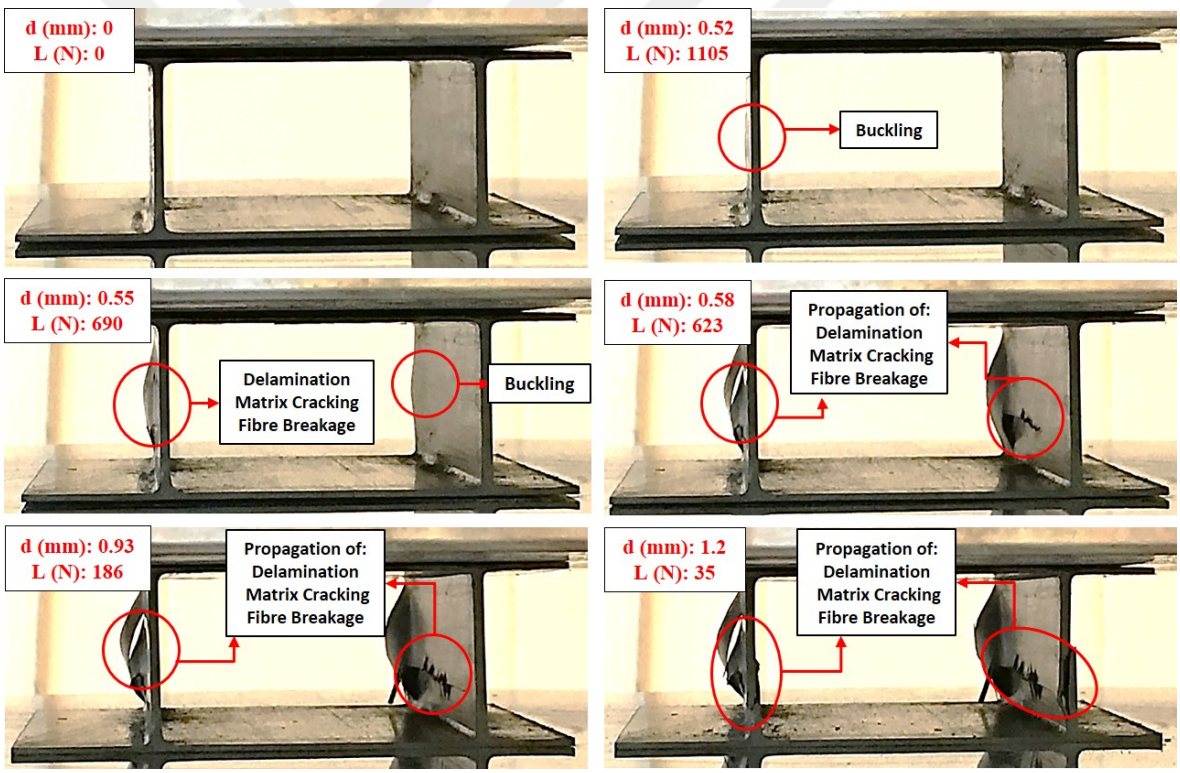


Figure 5.2: Failures in 2nd compression test

FEA predictions for damage patterns are summarized in Figures 5.3 and 5.4. It is seen that damage initiates with rib buckling at a displacement of 0.5 mm. This is where first major load drop is seen.

At the same displacement level, delamination initiates at rib-facesheet intersection along with fibre breaks in 90° plies (see Figure 5.3) and matrix cracks in 0° plies (see Figure 5.4). The difference between tests and FEA is that delamination and in-ply failures are close to rib-facesheet intersection in FEA. Then, secondary local buckling occurs close to the rib-facesheet intersection at a displacement of 0.55-0.6 mm and this is where second major load drop is observed. At the same duration, fibre breaks in 90° plies and matrix cracks in 0° plies propagate along with delamination initiation at buckle zone. Propagation of all delaminations, fibre breaks and matrix cracks continues by the end of simulation as seen in Figures 5.3 and 5.4.

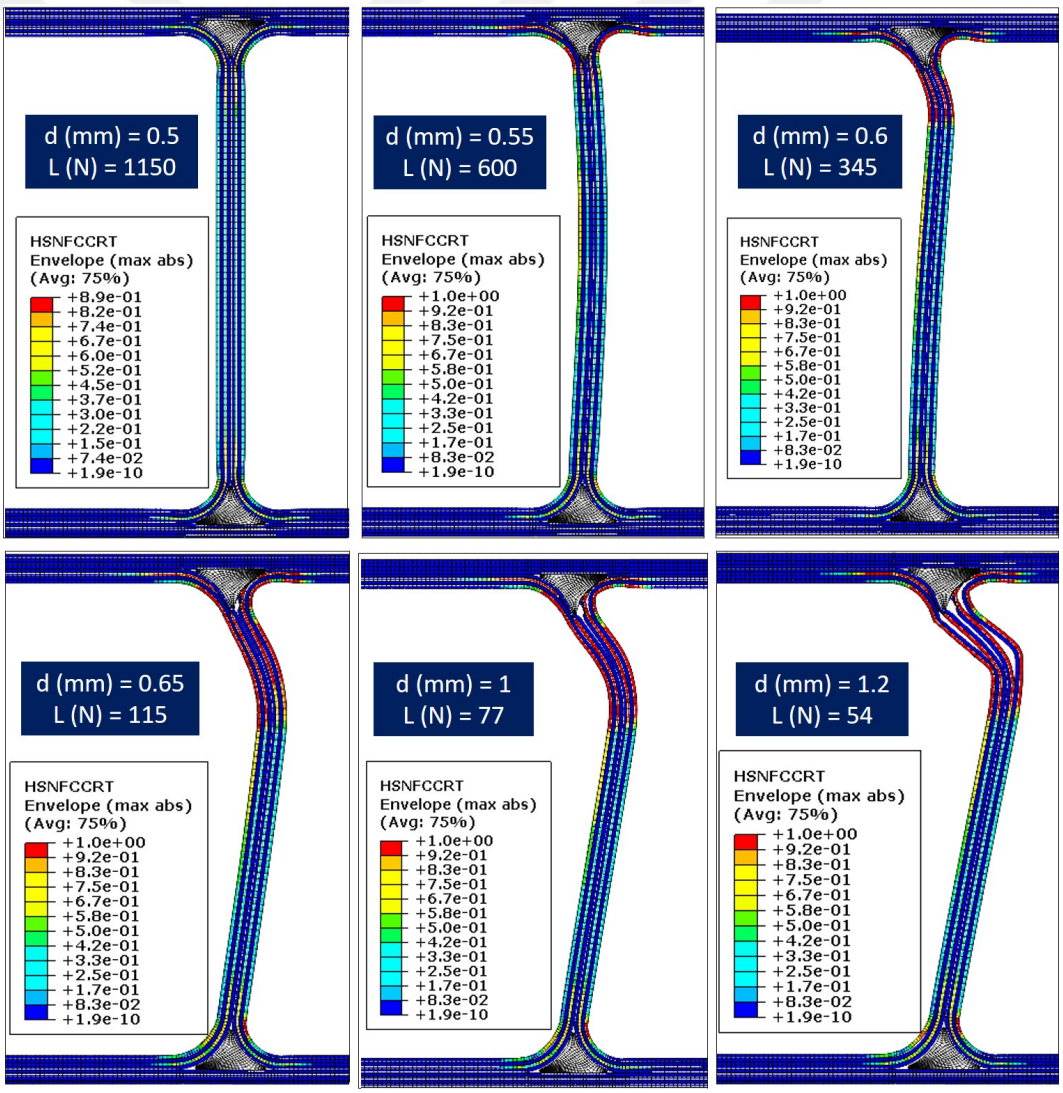


Figure 5.3: Delamination and Hashin's fibre compressive damage

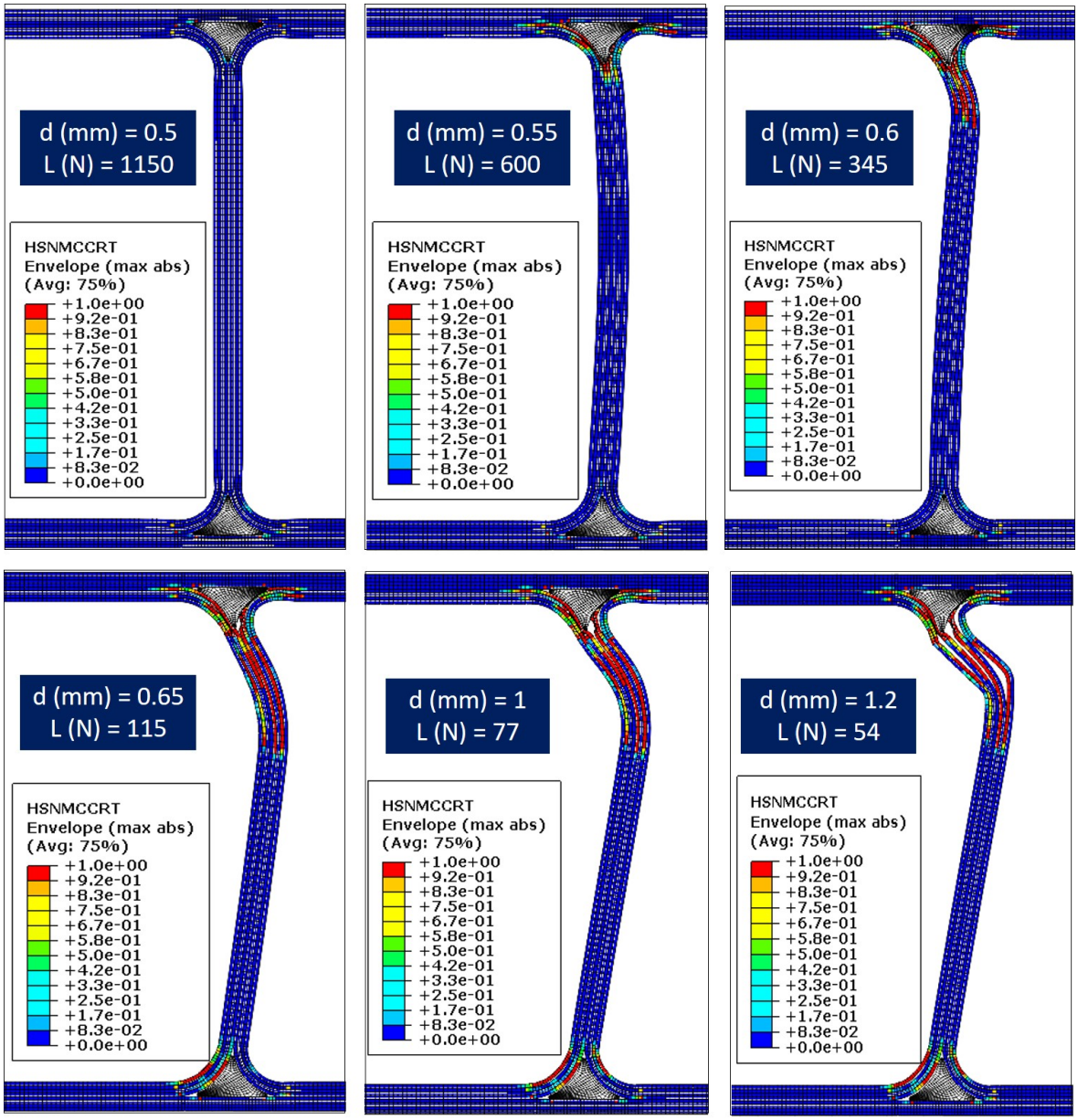


Figure 5.4: Delamination and Hashin's matrix compressive damage

Compression test and simulation load-displacement curves are demonstrated in Figure 5.5. It is seen that buckling is the dominant failure mechanism which determines load-carrying capacity of the structure. Buckling failure initiates at a displacement of 0.48 mm in 1st compression test and at a displacement of 0.51 mm in 2nd compression test. On the other hand, the same failure occurs at a displacement of 0.5 mm in FEA. This is where the first major load drop occurs and there is close match between test and simulation.

Furthermore, second major load drop occurs at a displacement of 0.53 mm in 1st compression test, at a displacement of 0.55 mm in 2nd compression test and at a displacement of 0.55 mm in FEA. After that point, test results show that the structure loses most of its load-carrying capacity and this trend matches with load-displacement curve of FEA.

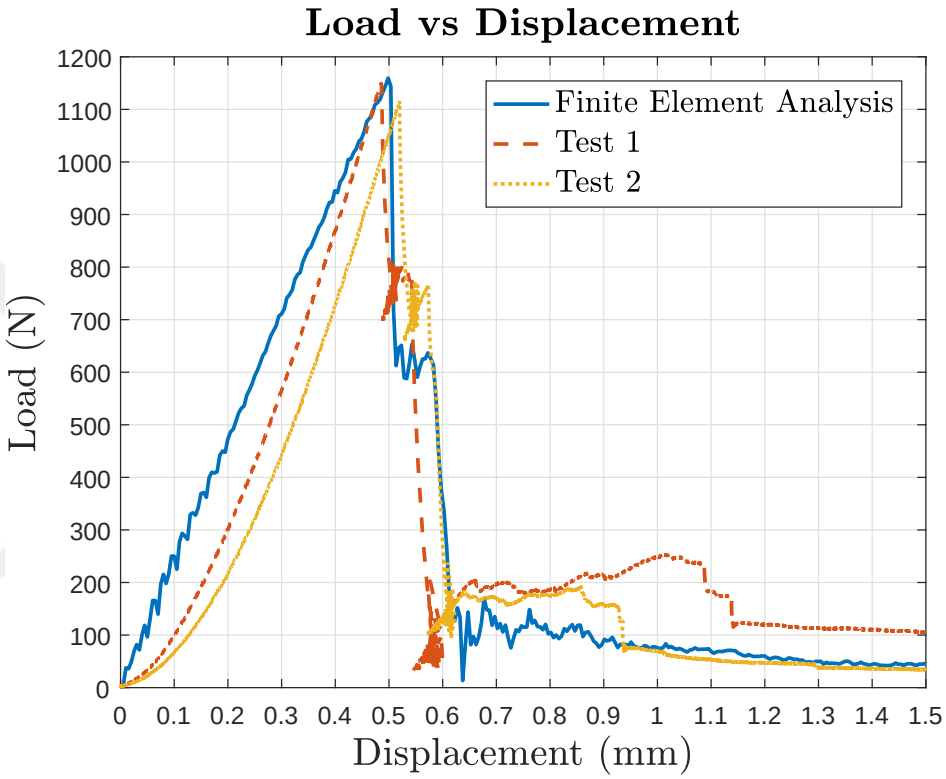


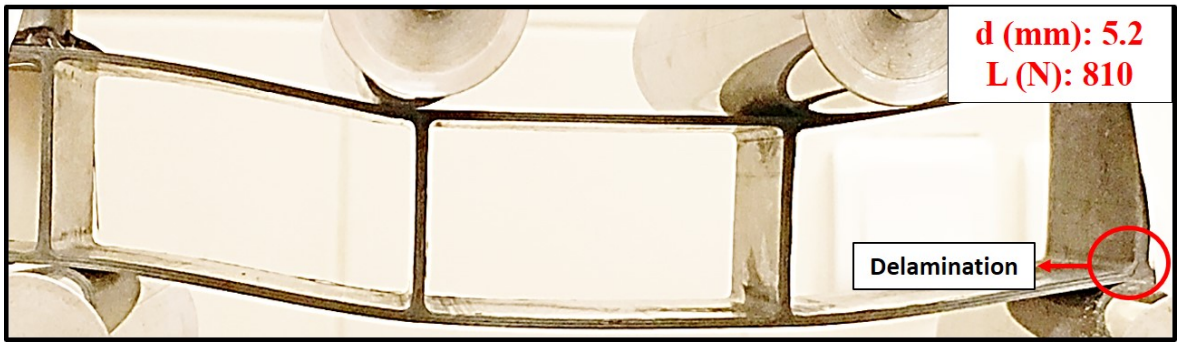
Figure 5.5: Load-displacement curves obtained in compression tests and FEA simulation

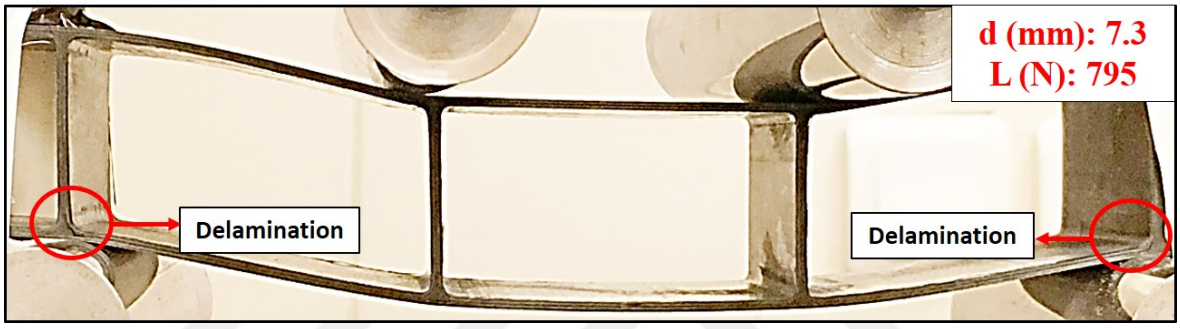
Comparing compression tests and simulation results, it can be said that failure patterns predicted by simulation is similar to those observed in compression tests. However, inconsistencies between test and simulation such as in-ply and delamination failure locations are unavoidable. There are some possible reasons for that. Firstly, manufacturing defects such as fibre waviness are unavoidable and unpredictable factors which affect failure behaviour of composite structure. Although utmost care is taken during manufacturing to wrap the prepreg layers on the aluminium mandrels, there may be some slack in the wrap, which results an extra length around the mandrel which is taken by fibre waviness during manufacturing under compression.

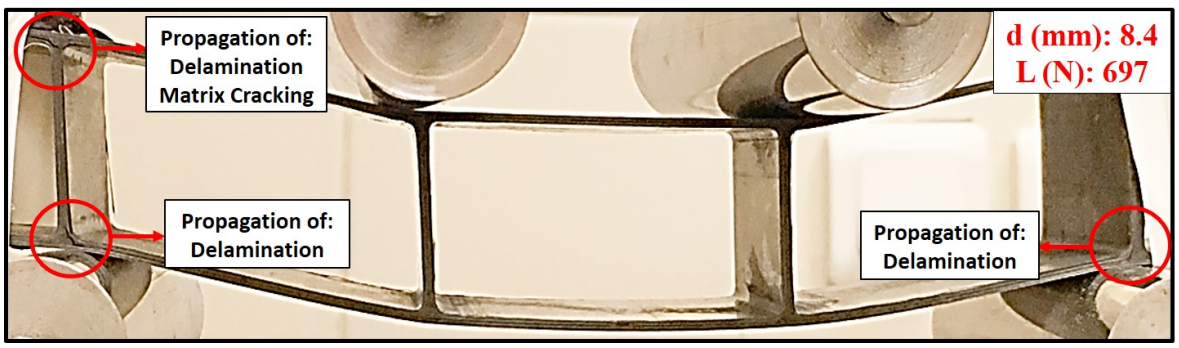
Fibre misalignment due to waviness reduces mechanical properties such as stiffness and strength [49]. Therefore, it is expected that buckling starts at rib zone which has fibre waviness defect. Since, fibre waviness location can be anywhere on rib plies, buckling and delamination might be observed in different locations of rib section. The other manufacturing defect, voids, induces a severe degradation of mechanical performance of the structure. Voids might arise due to moisture, volatile resin components, inadequate values of temperature-pressure during curing and tearing in vacuum bag [50]. Another composite manufacturing defect might be warpage. It refers to the inconsistency between the ideal and manufactured distorted shape. It occurs due to residual stress build-up during curing process. The distorted geometry has huge impact on load distribution on structure. Therefore, failure locations might be different in samples exposed to such defect.

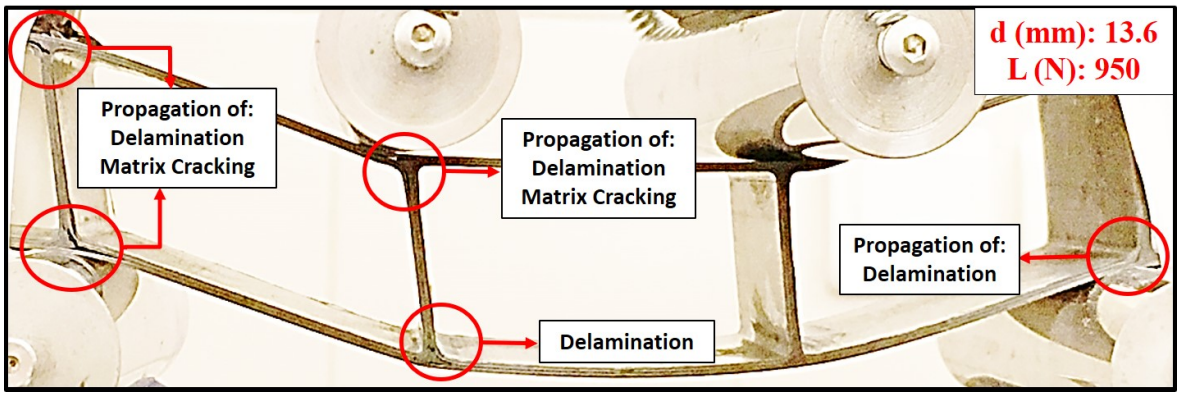
5.2. Four-Point Bending Test and FEA

Failure mechanisms in 1st four-point bending test are illustrated in Figure 5.6. Delamination is the first observed failure mode and it initiates around the bottom corner of right rib section at a displacement of 5.2 mm. This is the cause of first major load drop. Delamination initiates also around the bottom corner of left rib section at a displacement of 7.3 mm. Next delamination initiates around top corner of left rib section at a displacement of 8.4 mm. At the same displacement level, matrix cracking occurs in the 0° plies around the top corner of left rib section. As load rollers bend the structure further, new delaminations initiate and existing delaminations propagate. Furthermore, matrix cracks initiate and propagate around various rib-facesheet intersections. As seen in Figure 5.6, fibre breaks in the 90° plies are also observed through-the-thickness direction around the bottom corner of rib sections starting at a displacement of 19 mm. All delaminations, matrix cracks and fibre breaks propagate by the end of test.


d (mm): 5.2
L (N): 810
Delamination


d (mm): 7.3
L (N): 795
Delamination
Delamination


d (mm): 8.4
L (N): 697
Propagation of:
Delamination
Matrix Cracking
Propagation of:
Delamination
Propagation of:
Delamination


d (mm): 13.6
L (N): 950
Propagation of:
Delamination
Matrix Cracking
Propagation of:
Delamination
Matrix Cracking
Propagation of:
Delamination
Delamination

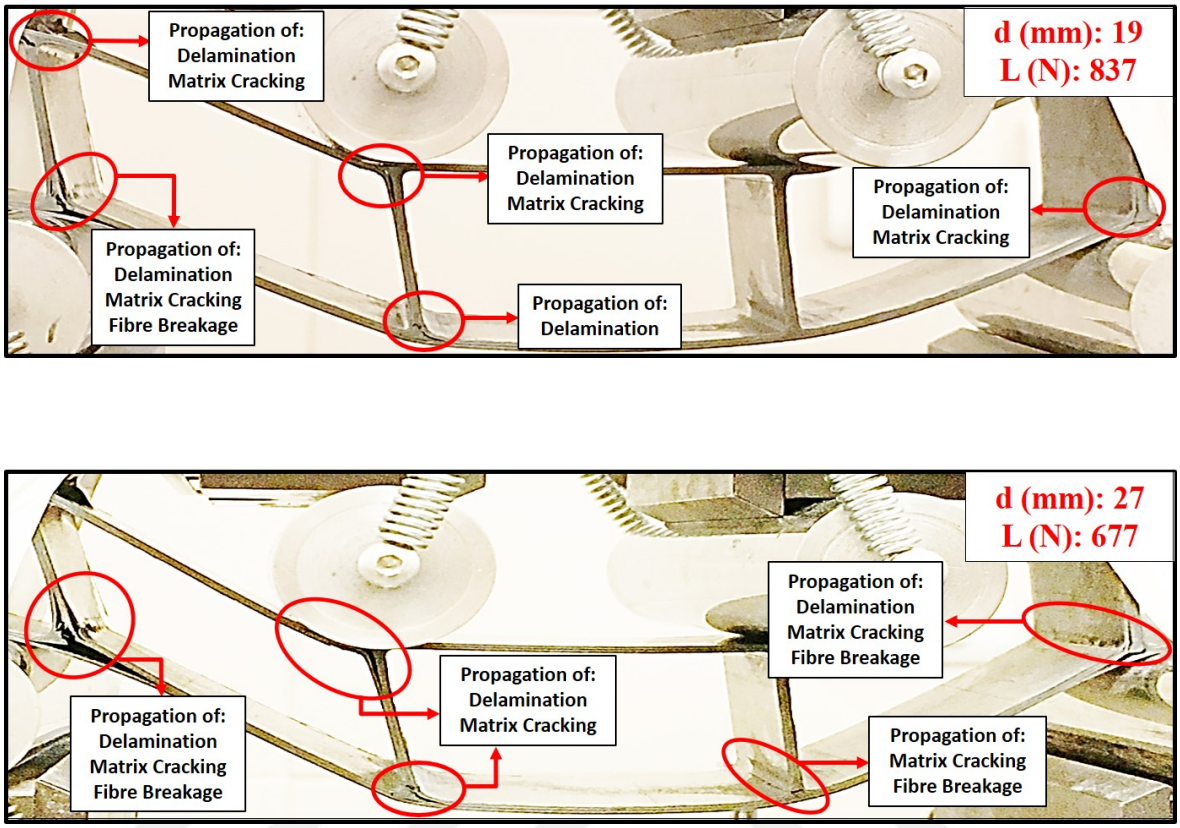
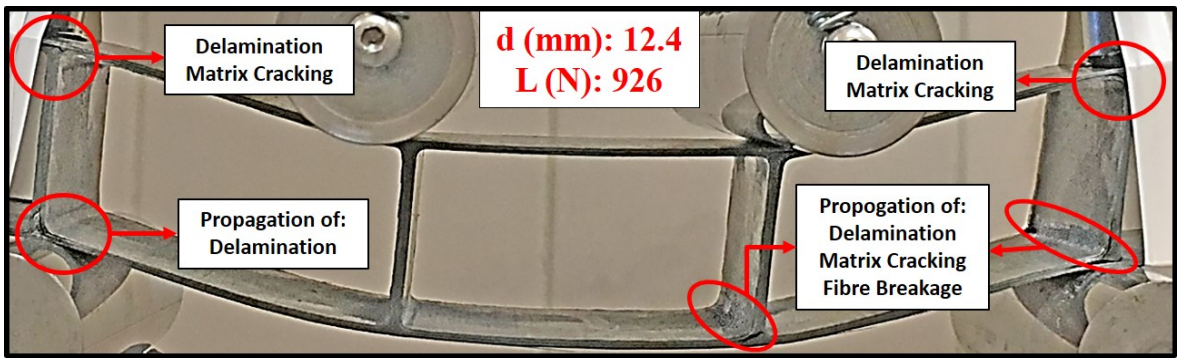


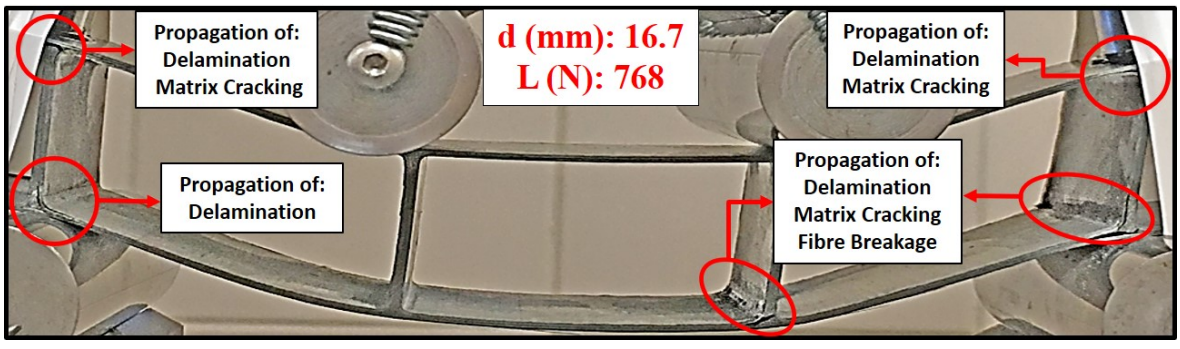
Figure 5.6: Failures in 1st four-point bending test

Failure mechanisms in 2nd four-point bending test are illustrated in Figure 5.7. It is observed that the failure modes in 2nd four-point bending test are similar to the 1st four-point bending test. The first observed delamination failure initiates around the bottom corner of right rib section at a displacement of 4.5 mm. This is the cause of first major load drop. Next delamination initiation occurs around the bottom corner of left rib section at a displacement of 10.8 mm. At a displacement of 12.4, matrix cracking starts around various rib-facesheet intersections. As load rollers bend the structure further, new delaminations initiate and existing delaminations propagate. Furthermore, matrix cracks initiate and propagate around various rib-facesheet intersections. As seen in Figure 5.7, fibre breaks in the 90° plies are also observed through-the-thickness direction around the bottom corner of rib sections starting at a displacement of 12.4 mm. All delaminations, matrix cracks and fibre breaks propagate by the end of test.


d (mm): 4.5
L (N): 855
Delamination


d (mm): 10.8
L (N): 835
Delamination
Propagation of:
Delamination


Delamination
Matrix Cracking
d (mm): 12.4
L (N): 926
Delamination
Matrix Cracking
Propagation of:
Delamination
Propogation of:
Delamination
Matrix Cracking
Fibre Breakage


Propagation of:
Delamination
Matrix Cracking
d (mm): 16.7
L (N): 768
Propagation of:
Delamination
Matrix Cracking
Propagation of:
Delamination
Propagation of:
Delamination
Matrix Cracking
Fibre Breakage

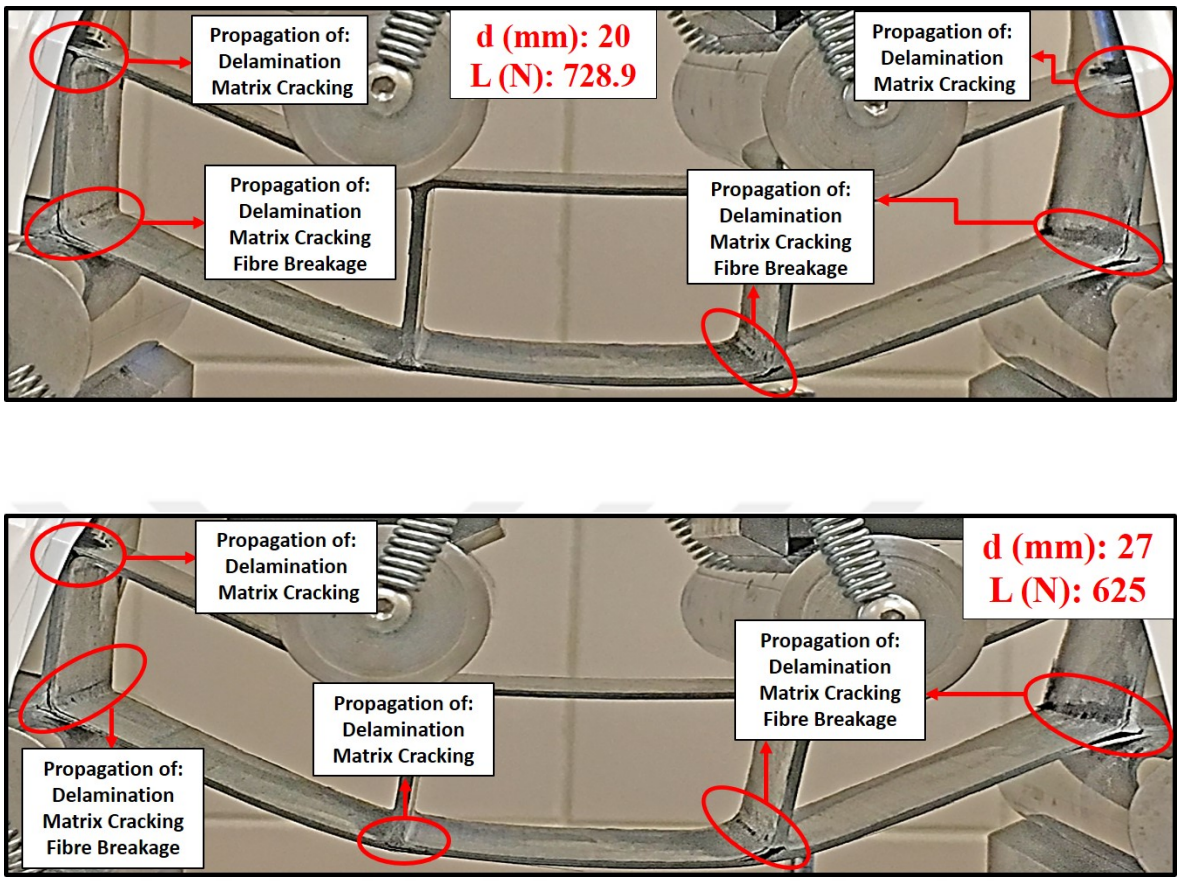
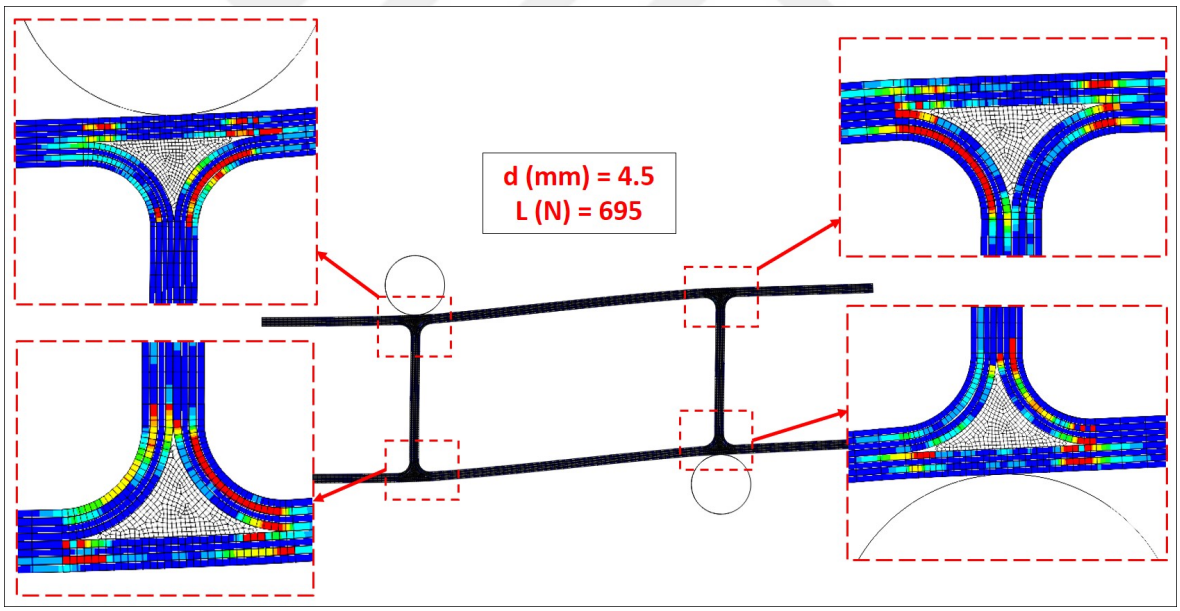
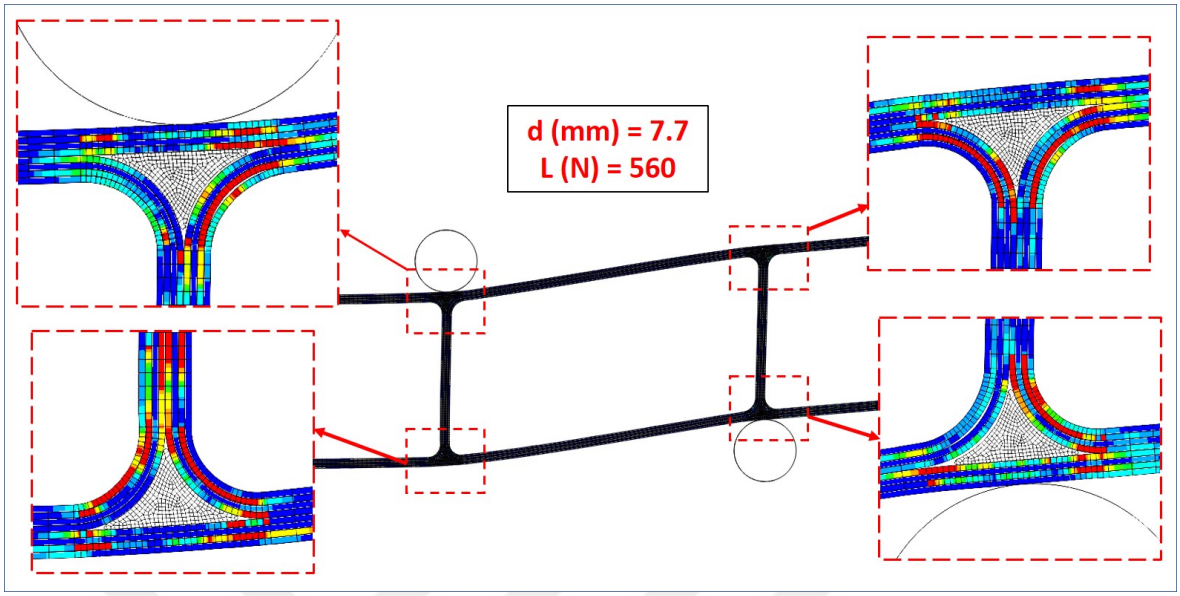


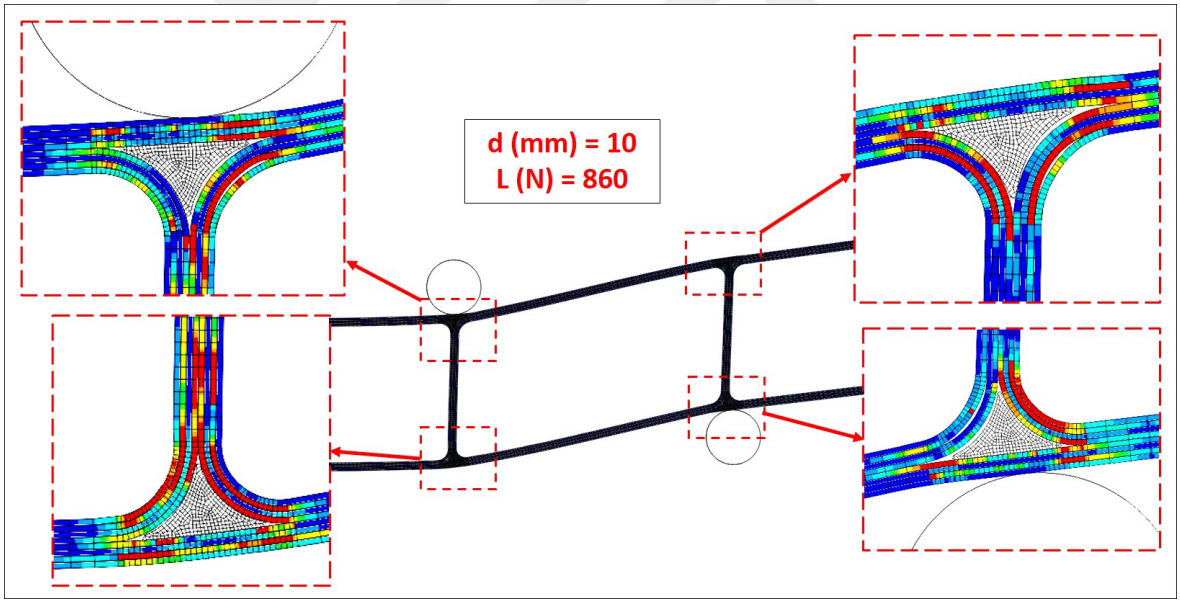
Figure 5.7: Failures in 2nd four-point bending test

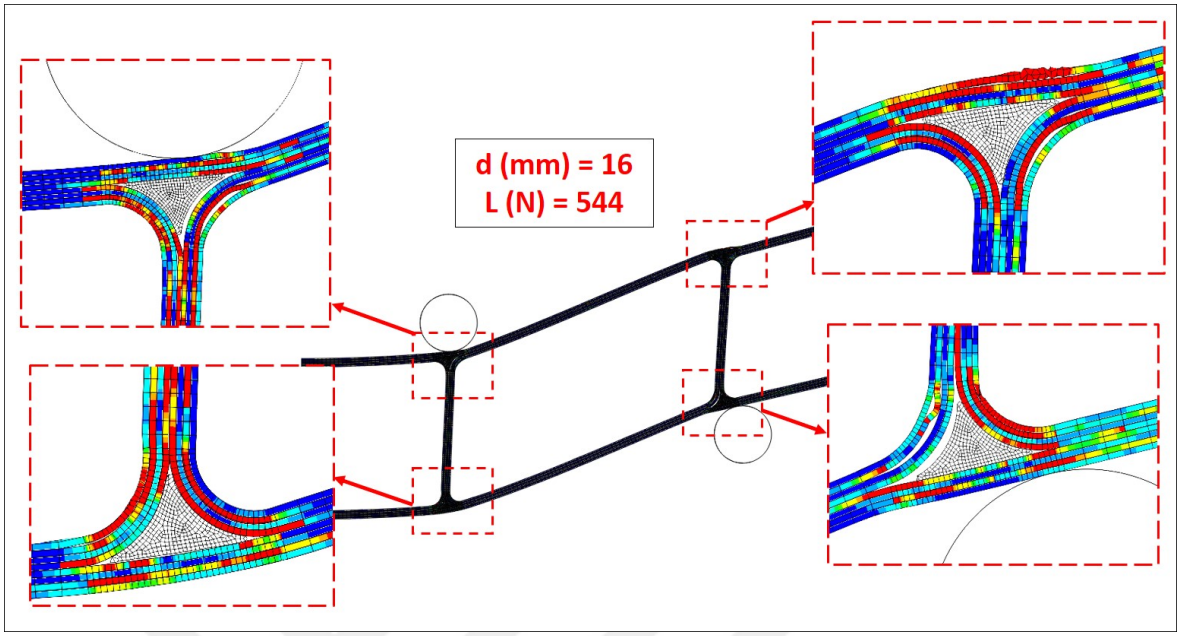
The progressive failure behaviour obtained by FEA is illustrated in Figure 5.8 and 5.9. Since rib-facesheet intersection surfaces are the main weak areas of the structure in four-point bending test loading condition, these areas are investigated further in detail. The first major load drop occurs at a displacement of 4.5 mm due to excessive matrix tensile failure in the 0° plies (see Figure 5.8) and also the delamination initiation around the top corner of the middle rib section as well as the bottom corner of the right rib section. Other failure modes are not initiated at this displacement level yet. At a displacement of 7.7 mm, the next delamination occurs around the top corner of the right rib section. Along with that, matrix tensile failures in the 0° plies and existing delaminations propagate as seen in Figure 5.8. FE predictions for fibre tensile failure are not as accurate as the matrix tensile failure and the delamination propagations.

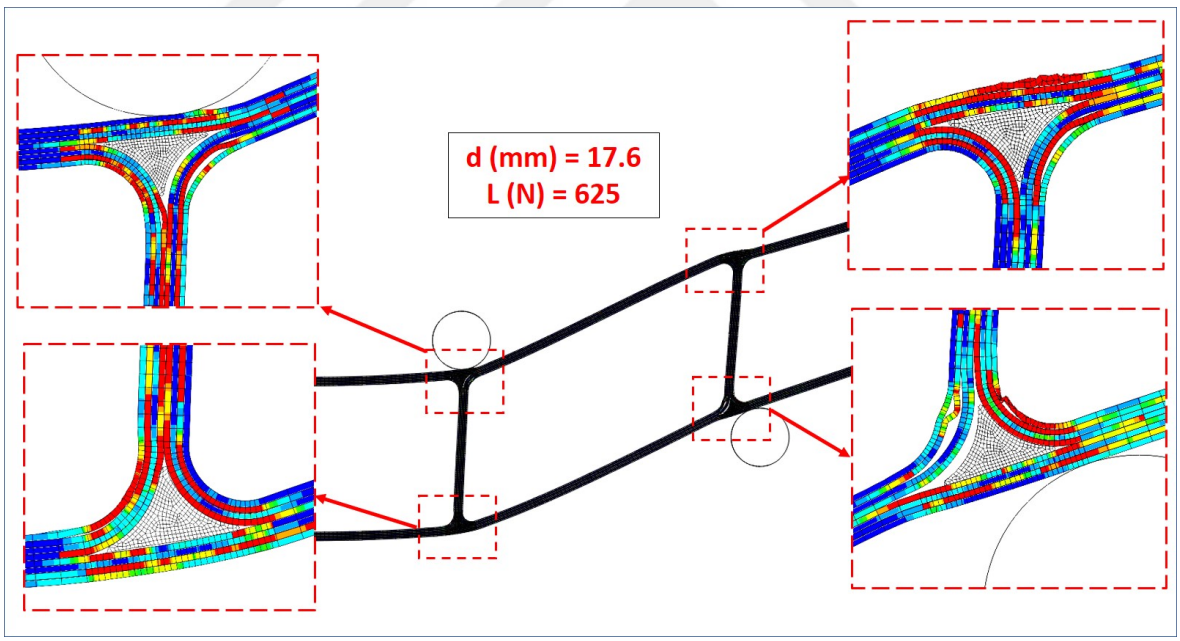
Fibre tensile failure onset and propagation starts in the 90° plies at a displacement of 10 mm as shown in Figure 5.9. It is seen that this failure mode occurs at elements located in acute side of bottom corner of the right rib section. These elements are already exposed to excessive matrix failure and excessive distortion. Therefore they are removed from stiffness matrix in FEA. This might be a reason for unexpected fibre failure mode for the elements located in acute side. The expected fibre tensile failure starts in the 90° plies at a displacement of 10 mm for elements located in obtuse side of bottom corner of the middle rib section and at a displacement of 16 mm for elements located in obtuse side of bottom corner of the right rib section. After that point, as the load rollers bend the structure further, all delaminations, matrix tensile failures in the 0° plies and fibre tensile failures in the 90° plies propagate by the end of simulation as seen in Figure 5.8 and 5.9.




d (mm) = 7.7
L (N) = 560


d (mm) = 10
L (N) = 860


d (mm) = 16
L (N) = 544


d (mm) = 17.6
L (N) = 625

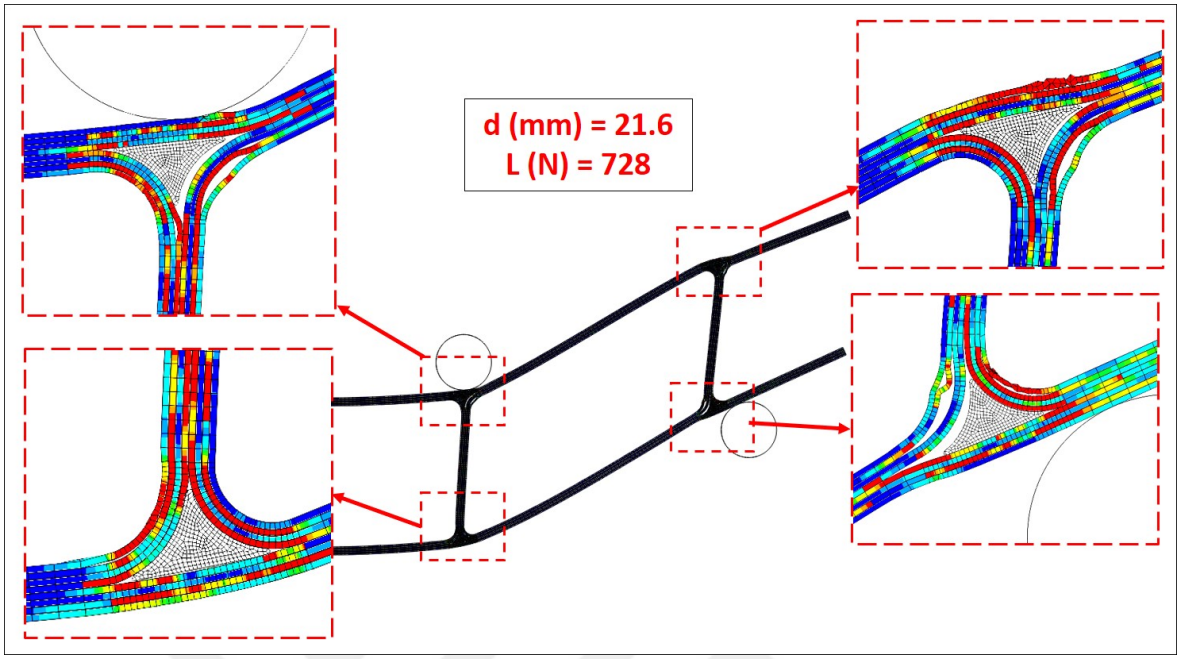
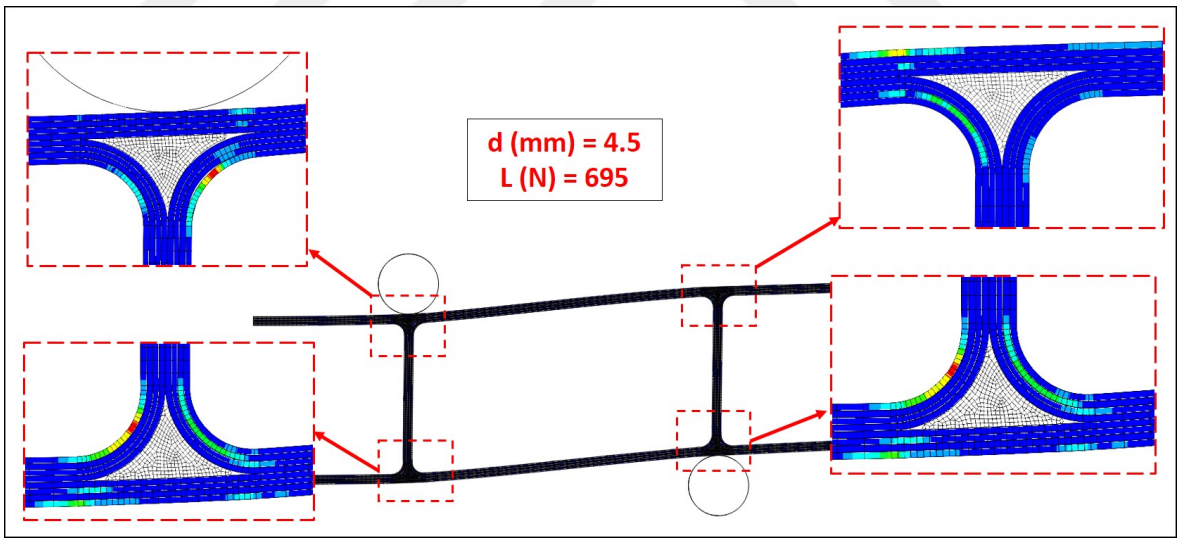
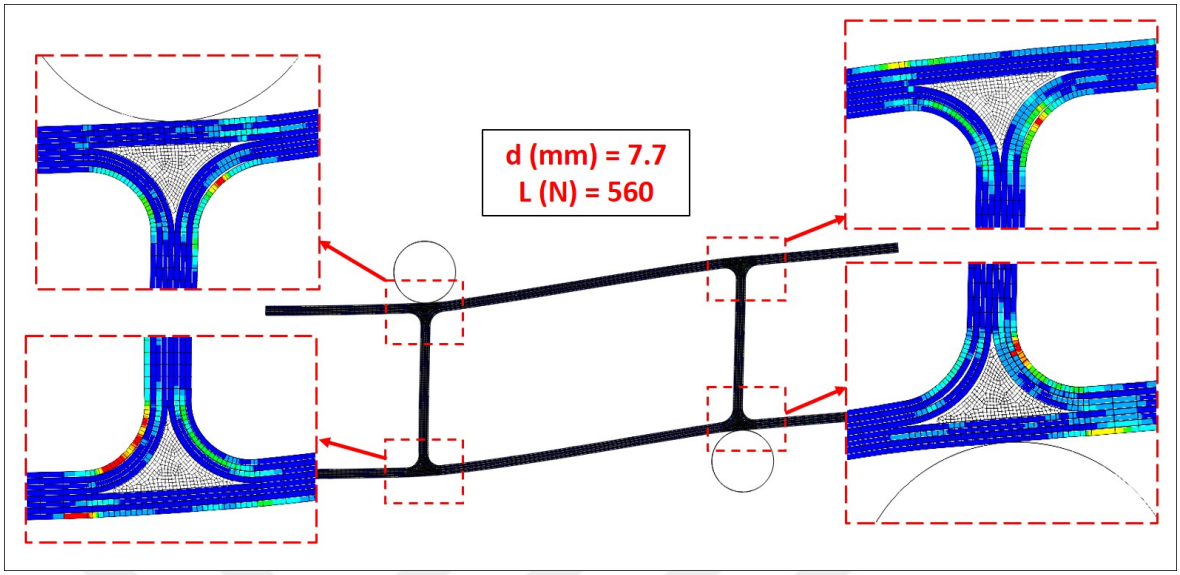
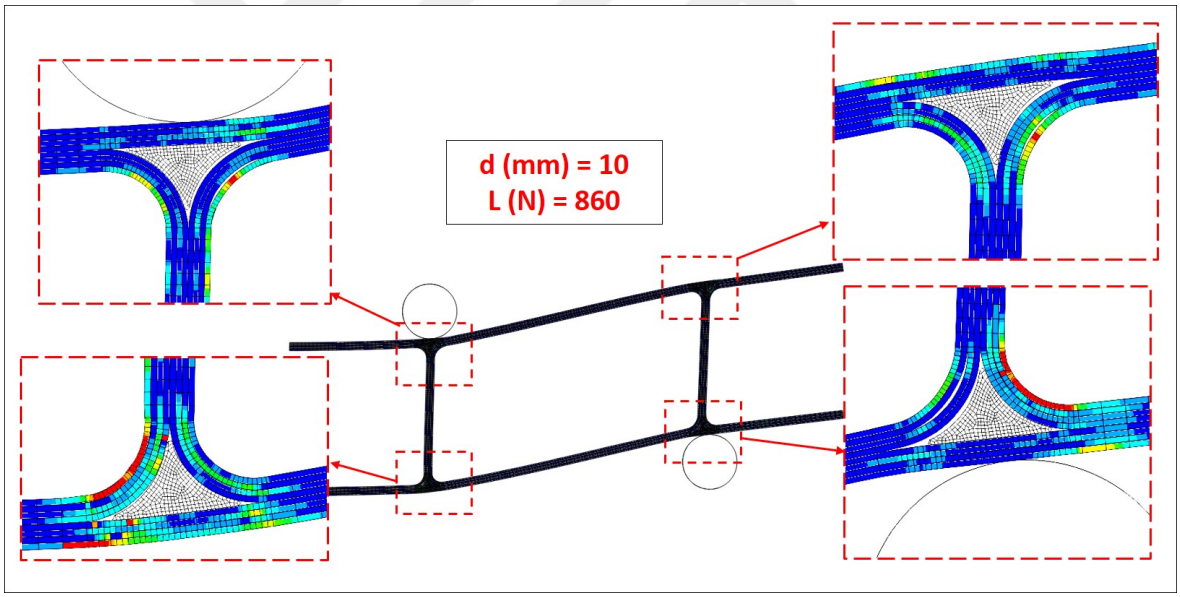
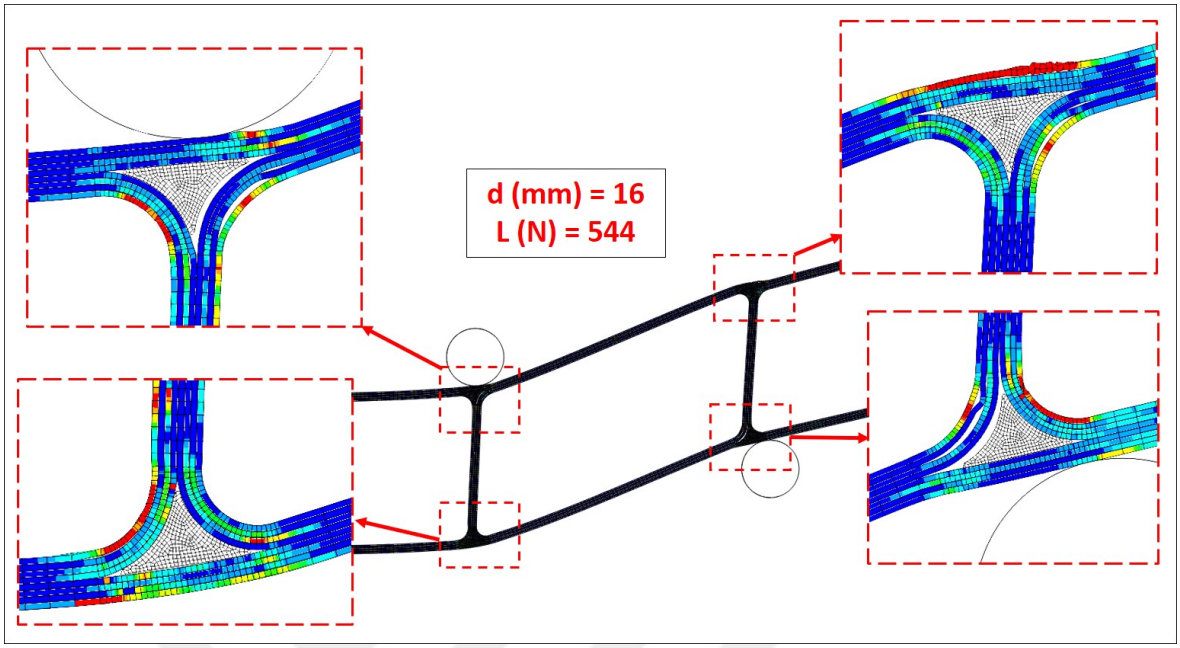


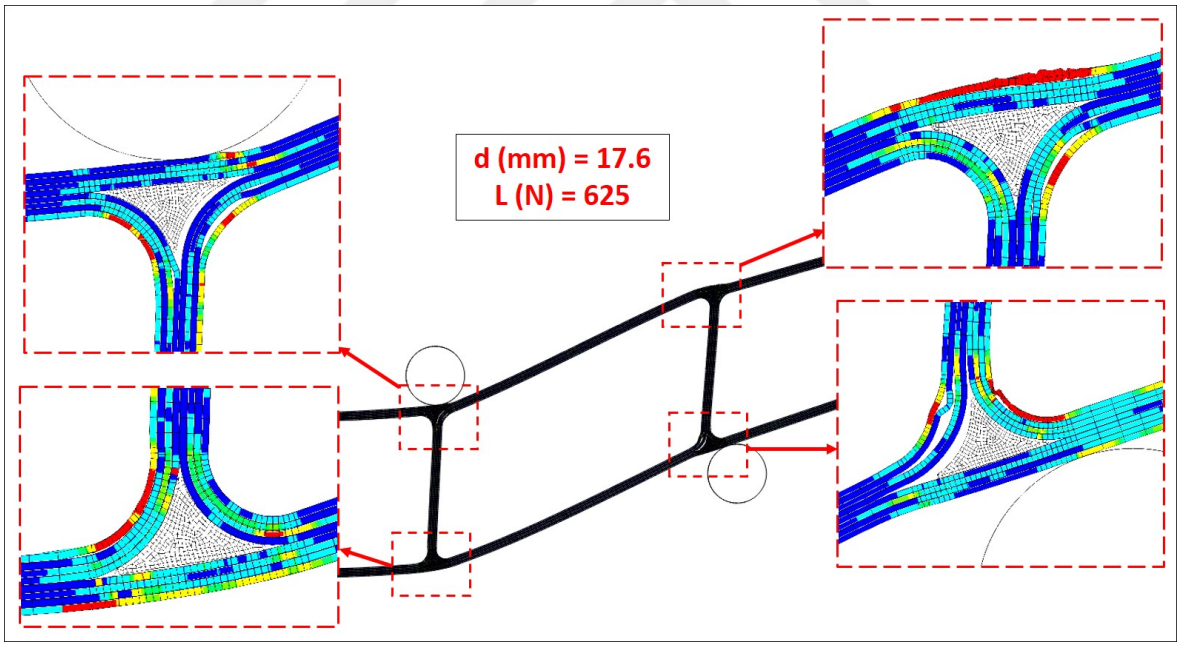
Figure 5.8: Delamination and matrix tensile damages in 4-point bending test simulation




d (mm) = 7.7
L (N) = 560


d (mm) = 10
L (N) = 860


d (mm) = 16
L (N) = 544


d (mm) = 17.6
L (N) = 625

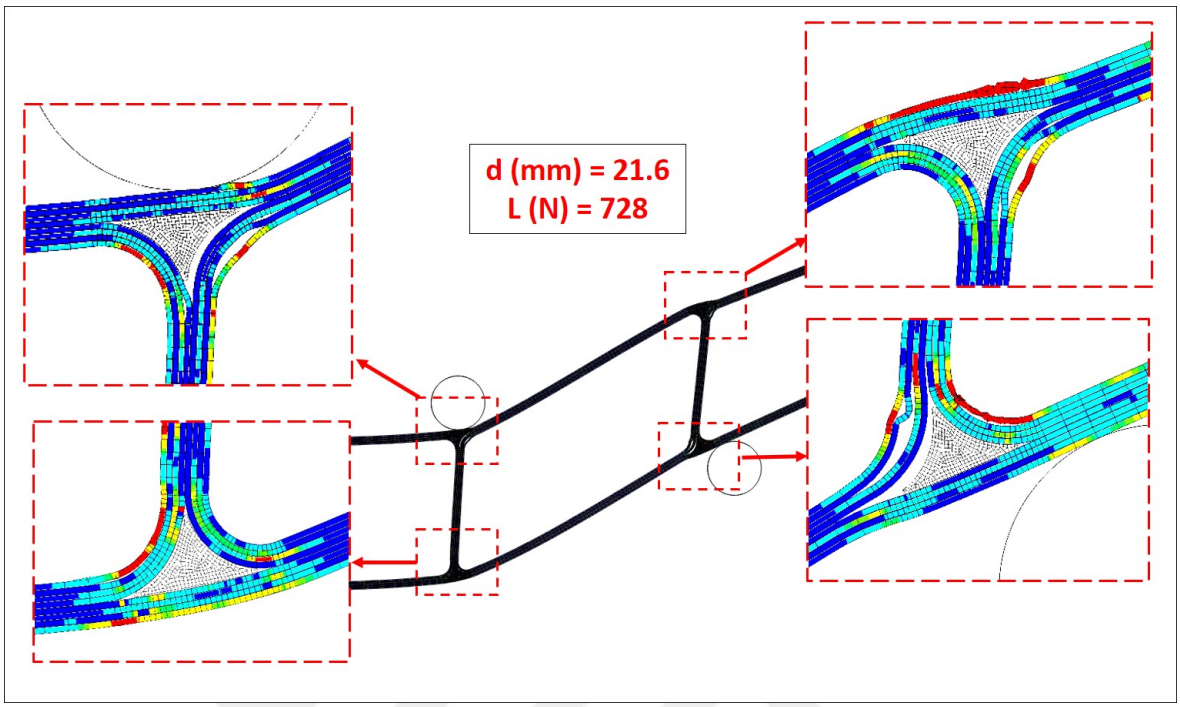


Figure 5.9: Delamination and fibre tensile damages in 4-point bending test simulation

The load-displacement curve obtained by FEA is compared with experimental results in Figure 5.10. It is seen that load increases linearly along with up to 4-5 mm displacement. Then, there is a major drop in load level as a result of first delamination initiation around rib-facesheet intersection and there is a close match between test and simulation. After that point, as displacement increases, load increases as well up to next damage. When Hashin's damage initiates for an element or delamination failure grows, load decreases again. This trend continues until that the total displacement reaches to 30 mm. It can be said that although it is not possible to exactly predict the successive load drops after the first failure in FEA, the general trend in load-displacement curve after first delamination initiation is also predicted reasonably well.

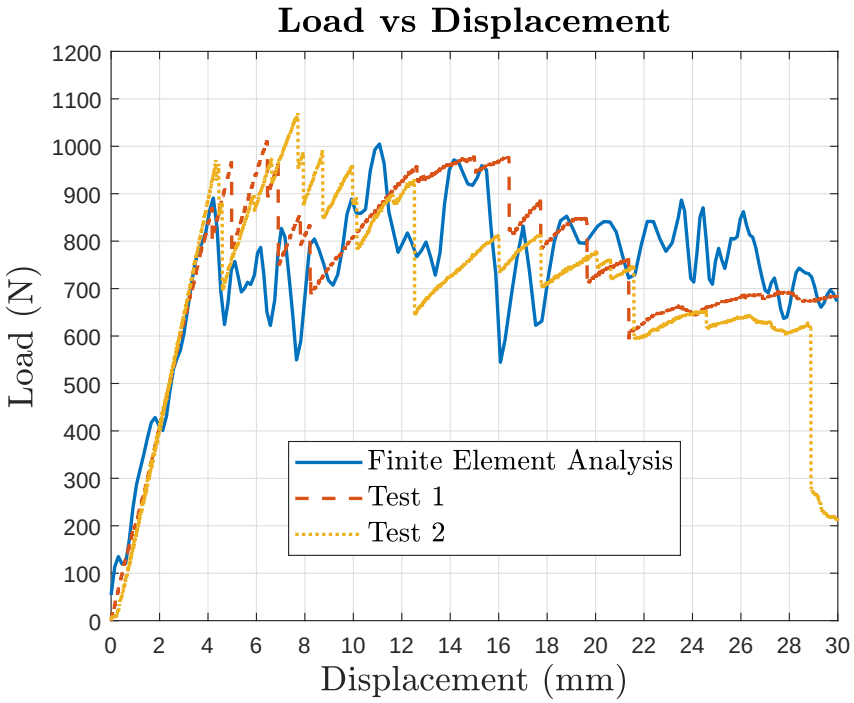


Figure 5.10: Load-displacement curves obtained in 4-point bending tests and FEA simulation

Comparing four-point bending tests and simulation results, it can be said that failure patterns predicted by simulation is similar to failure patterns observed in four-point bending tests. Naturally, there are small variances between simulation and test results in terms of failure time and amount of damage area. As it is indicated in compression test results discussion, some manufacturing defects such as fibre waviness, voids and warpage might have direct impact on sample's ability to carry load. Especially geometric distortion due to warpage defect might lead load distribution on four-point bending test sample to be quite different than predicted one because simulation is conducted by assuming perfect sample geometry. Therefore, some zones in test samples are exposed to stress higher than prediction and experience damage first. Another very important parameter is the reliability of tools and fixture. In four-point bending test set-up, rollers are supported by spring mechanisms in transverse direction. Relaxation of these springs cause rollers not to align perfectly parallel to test sample, which has impact on load distribution on test sample.

This might be another reason for variations between simulation and test results. Other reason for the differences between simulation and test results is that Hashin's Failure Criterion is not investigated for deltoid section. In four-point bending test loading condition, major load is carried by rib-facesheet intersection zones. Although deltoid section is a very small area compared to whole structure, ignoring in-ply failures for this section might make the structure stiffer than it normally is and adversely affects simulation accuracy. Last difference between FEA and test results is that fibre tensile failure occurs at elements in acute side of bottom corner of right rib section. These elements are already exposed to excessive matrix failure and excessive distortion. Therefore, they are already removed from stiffness matrix. This might be the reason for observing unexpected fibre tensile failure in the elements located in acute side.

6. CONCLUSIONS AND FUTURE WORK

In this study, progressive failure analysis of a corrugated core type composite sandwich structure is performed both experimentally and numerically. Two different types of structure are manufactured depending on core cell numbers. Structures with one core cell are used in compression test and structures with three core cells are used in four-point bending test. Finite Element Model is developed in ABAQUS/Explicit to simulate these tests and predict failure response of structures under different loading conditions.

In-ply damages are investigated by Hashin's Failure Criterion, which is the default damage initiation criterion in ABAQUS. On the other hand, initiation and evolution of delamination failure are simulated based on Cohesive Zone Model (CZM). CZM is defined in ABAQUS by introducing Interaction Properties, mainly interfacial fracture strength, fracture energy and penalty stiffness values for each failure mode. Both compression and four-point bending tests are simulated separately. Numerical results are validated with experiments by comparing failure mechanisms and load-displacement curves of both compression and four-point bending test simulations.

In FE model, deltoid sections of structure are meshed with solid element instead of continuum shell element. Since Hashin Criterion is not defined in solid element, deltoid section is not investigated in terms of in-ply damages. As a future work, VUMAT code can be developed to define Hashin Failure Criterion by using solid element. Furthermore, other in-ply damage criteria such as Tsai-Wu and Tsai-Hill can be also implemented to ABAQUS software via VUMAT code. In this way, accuracy of various damage criteria can be compared to each other. Another future work might be to perform interlaminar analysis by using cohesive element method instead of cohesive surface method. In cohesive element method, additional very thin layer is defined between interaction surfaces of adjacent plies. These two methods might be compared to each other in terms of accuracy and run time.

REFERENCES

1. Association, E. A. M., *Road transport: Reducing CO2 emissions from vehicles*, 2017, https://ec.europa.eu/clima/policies/transport/vehicles/, accessed at June 2018.

2. Mazumdar, S., *Growth Opportunities in Global Composites Industry*, Lucintel, 2012, https://www.compositesworld.com/columns/how_to_win_in_carbon_composites_for_the_automotive_market, accessed at June 2018.

3. Abliz, D., Y. Duan, L. Steuernagel, L. Xie, D. Li and G. Ziegmann, "Curing Methods for Advanced Polymer Composites - A Review", *Polymers and Polymer Composites*, Vol. 21, pp. 341–348, 01 2013.

4. Aly, N., "A review on utilization of textile composites in transportation towards sustainability", *IOP Conference Series: Materials Science and Engineering*, Vol. 254, No. 4, p. 042002, 2017.

5. Mazumdar, S., *A global outlook at materials and markets for composites*, Lucintel, 2018, http://compositesmanufacturingmagazine.com/2018/01/2018_composites_manufacturing_state_of_the_industry_report/, accessed at June 2018.

6. Thomsen, O., "Sandwich Materials for Wind Turbine Blades – Present and Future", *Sandwich Structures and Materials*, Vol. 11, pp. 7–26, 01 2009.

7. Reddy, J., *Mechanics of Laminated Composite Plates and Shells: Theory and Analysis, Second Edition*, Taylor & Francis, 2004.

8. Rahman, A. and M. Gibson, *Effectiveness of Honeycomb Structure in Main Battle Tank Design*, M.Sc. Thesis, Cranfield University, 07 2013.

9. Group, W. R., *Ultralight Cellular Materials*, University of Virginia, `http://www.virginia.edu/ms/research/wadley/celluar-materials.html`, accessed at June 2018.

10. Wang, B., G. Zhang, Q. He, L. Ma, L. Wu and J. Feng, "Mechanical behavior of carbon fiber reinforced polymer composite sandwich panels with 2-D lattice truss cores", *Materials and Design*, Vol. 55, No. Supplement C, pp. 591–596, 2014.

11. Xu, G., J. Zhai, T. Zeng, Z. Wang, S. Cheng and D. Fang, "Response of composite sandwich beams with graded lattice core", *Composite Structures*, Vol. 119, No. Supplement C, pp. 666–676, 2015.

12. Rejab, M. and W. Cantwell, "The mechanical behaviour of corrugated-core sandwich panels", *Composites Part B: Engineering*, Vol. 47, pp. 267–277, 2013.

13. Xu, G., Z. Wang, T. Zeng, S. Cheng and D. Fang, "Mechanical response of carbon/epoxy composite sandwich structures with three-dimensional corrugated cores", *Composites Science and Technology*, Vol. 156, pp. 296–304, 2018.

14. Zhang, J., P. Supernak, S. Alander and C. Wang, "Improving the bending strength and energy absorption of corrugated sandwich composite structure", *Materials and Design*, Vol. 52, pp. 767–773, 2013.

15. Wu, Z., W. Liu, L. Wang, H. Fang and D. Hui, "Theoretical and experimental study of foam-filled lattice composite panels under quasi-static compression loading", *Composites Part B: Engineering*, Vol. 60, pp. 329–340, 2014.

16. Fan, H., F. Meng and W. Yang, "Sandwich panels with Kagome lattice cores reinforced by carbon fibers", *Composite Structures*, Vol. 81, No. 4, pp. 533–539, 2007.

17. Jin, F., H. Chen, L. Zhao, H. Fan, C. Cai and N. Kuang, "Failure mechanisms of sandwich composites with orthotropic integrated woven corrugated cores: Experi-

ments", *Composite Structures*, Vol. 98, No. Supplement C, pp. 53–58, 2013.

18. Fan, H., Z. Qu, Z. Xia and F. Sun, "Designing and compression behaviors of ductile hierarchical pyramidal lattice composites", *Materials and Design*, Vol. 58, No. Supplement C, pp. 363–367, 2014.

19. Cinar, K., F. Oz and N. Ersoy, "Failure Behavior of Corrugated Core Panel Under Out-of-plane Loading", *20th International Conference on Composite Materials*, 07 2015.

20. Hyer, M. and S. White, *Stress Analysis of Fiber-reinforced Composite Materials*, DEStech Publications, Virginia Polytechnic Institute and State University, 2009.

21. Prasad, R., *Delamination*, Heidelberg India, 2014, `https://www.slideshare.net/heidelbergindia9/slides-on-delamination`, accessed at June 2018.

22. Shipsha, A. and D. Zenkert, "Compression-after-Impact Strength of Sandwich Panels with Core Crushing Damage", *Applied Composite Materials*, Vol. 12, pp. 149–164, 05 2005.

23. Uzal, A., F. Sonmez, F. Oz, K. Cinar and N. Ersoy, "A composite sandwich plate with a novel core design", *Composite Structures*, Vol. 193, pp. 198–211, 2018.

24. Heimbs, S., P. Middendorf and M. Maier, "Honeycomb Sandwich Material Modeling for Dynamic Simulations of Aircraft Interior Components", pp. 1–20, 06 2006.

25. Sleight, D. and L. R. Center, *Progressive failure analysis methodology for laminated composite structures*, Springfield, Langley Research Center, 1999.

26. Inc., A., "Abaqus Lecture 9: Material Damage and Failure", *Abaqus 6.11 Analysis User's Manual*, pp. 1–19, 2005.

27. Paris, F. and K. Jackson, *A Study of Failure Criteria of Fibrous Composite Materials*, Langley Research Center, George Washington University, 04 2001.

28. Tsai, S., *Strength Characteristics of Composite Materials*, National Aeronautics and Space Administration, Washington, D.C., 04 1965.

29. Systems, D., "Damage initiation for fiber-reinforced composites", *Abaqus 6.11 Analysis User's Manual*, 2011.

30. Systems, D., "Damage evolution and element removal for fiber-reinforced composites", *Abaqus 6.11 Analysis User's Manual*, 2011.

31. Wang, W., X. Wan, J. Zhou, M. Zhao, Y. Li, S. Shang and X. Gao, "Damage and Failure of Laminated Carbon-Fiber-Reinforced Composite under Low-Velocity Impact", *Journal of Aerospace Engineering*, Vol. 27, No. 2, pp. 308–317, 2014.

32. Systems, D., "SIMULIA Lecture 6: Surface-based Cohesive Behavior", *Abaqus 6.11 Analysis User's Manual*, pp. 1–36, 2011.

33. Moslemi, M. and M. Khoshravan, "Cohesive Zone Parameters Selection for Mode-I Prediction of Interfacial Delamination", *Strojniski Vestnik/Journal of Mechanical Engineering*, Vol. 61, pp. 507–516, 09 2015.

34. Benzeggagh, M. and M. Kenane, "Measurement of Mixed-Mode Delamination Fracture Toughness of Unidirectional Glass/Epoxy Composites with Mixed-Mode Bending Apparatus", *Composites Science and Technology*, Vol. 56, pp. 439–449, 04 1996.

35. Sokolinsky, V., K. Indermuehle and J. Hurtado, "Numerical simulation of the crushing process of a corrugated composite plate", *Composites Part A: Applied Science and Manufacturing*, Vol. 42, No. 9, pp. 1119–1126, 2011.

36. Turon, A., C. Dávila, P. Camanho and J. Costa, "An engineering solution for mesh size effects in the simulation of delamination using cohesive zone models", *Engineering Fracture Mechanics*, Vol. 74, pp. 1665–1682, 07 2007.

37. Moes, N. and T. Belytschko, "Extended finite element method for cohesive crack growth", *Engineering Fracture Mechanics*, Vol. 69, pp. 813–833, 05 2002.

38. Falk, M., A. Needleman and J. Rice, "A Critical Evaluation of Cohesive Zone Models of Dynamic Fracture", *Journal De Physique IV*, Vol. 11, pp. 43–50, 09 2001.

39. Harper, P. and S. Hallett, "Cohesive zone length in numerical simulations of composite delamination", *Engineering Fracture Mechanics*, Vol. 75, No. 16, pp. 4774–4792, 11 2008.

40. Moslemi, M. and M. Khoshravan, "Cohesive Zone Parameters Selection for Mode-I Prediction of Interfacial Delamination", *Strojniski Vestnik/Journal of Mechanical Engineering*, Vol. 61, pp. 507–516, 09 2015.

41. Zou, Z., S. Reid and S. Li, "Modelling interlaminar and intralaminar damage in filament-wound pipes under quasi-static indentation", *Journal of Composite Materials*, Vol. 36, No. 4, pp. 477–499, 2002.

42. Camanho, P., C. Dávila and M. Moura, "Numerical Simulation of Mixed-Mode Progressive Delamination in Composite Materials", *Journal of Composite Materials*, Vol. 37, pp. 1415–1438, 08 2003.

43. Turon, A., J. Costa, P. Camanho, P. Maimí, C. G. Dávila, S. Pinho and J. Remmers, *Analytical and Numerical Investigation of the Length of the Cohesive Zone in Delaminated Composite Materials*, Vol. 10, Springer Science, Netherlands, 2008.

44. Chen, J., E. Ravey, S. Hallett, M. Wisnom and M. Grassi, "Prediction of Delamination in Braided Composite T-Piece Specimens", *Composites Science and Technology*, pp. 2363–2367, 07 2009.

45. Inc., A., "Abaqus Lecture 5: Quasi-Static Analyses", *Abaqus 6.11 Analysis User's Manual*, pp. 1–33, 2005.

46. Cooperation, H., *HexPly ® 8552-Product Data Sheet*, 2016, `http://www.hexcel.com/user_area/content_media/raw/HexPly_8552_eu_DataSheet.pdf`, accessed at June 2018.

47. Ahmadvashaghbash, S., F. Oz, M. Mehdikhani, S. Lomov and N. Ersoy, "Experimental and Numerical Progressive Failure Analysis in Open-Hole Tensile Tests of Quasi-Isotropic Composite Laminates", *ECCM18-18th European Conference on Composite Materials*, 06 2018.

48. Ersoy, N., S. Ahmadvashaghbash, M. Engul and F. Oz, "A Comparative Numerical Study Aiming to Reduce Computation Cost for Mode-I Delamination Simulations", *ECCM18-18th European Conference on Composite Materials*, 06 2018.

49. Thirumalai, D., H. Lilholt, F. Aviles, L. Tom and H. Knudsen, "Fibre waviness and misalignment measurement of unidirectional glass/LPET commingled composites – Effect on mechanical properties", *Risoe International Symposium on Materials Science. Proceedings*, Vol. 34, pp. 349–363, 2013.

50. Soares, M., *Defects tracking in Out-of-Autoclave composite materials*, M.Sc. Thesis, University of Porto, 10 2017.